Energy & Environmental Science

ROYAL SOCIETY OF CHEMISTRY

REVIEW

View Article Online
View Journal | View Issue

Cite this: *Energy Environ. Sci.*, 2025, **18**, 5190

Water electrolysis technologies: the importance of new cell designs and fundamental modelling to guide industrial-scale development†

Muhammad Adil Riaz,[a] Panagiotis Trogadas, *[ad] David Aymé-Perrot,[b] Christoph Sachs,[b] Nicolas Dubouis,[b] Hubert Girault [c] and Marc-Olivier Coppens *[a]

Received 25th November 2024,
Accepted 24th April 2025

DOI: 10.1039/d4ee05559d

rsc.li/ees

Large-scale, sustainable, low-cost production of hydrogen can reduce the negative effects of climate change by decarbonising energy infrastructure. Low-carbon hydrogen can be synthesised *via* water electrolysis. Today, however, this only constitutes a minor proportion of global hydrogen production, as fossil fuel-based processes are used predominantly with large amounts of carbon emissions. Low-temperature electrolysis (<100 °C) has garnered significant attention, due to lower capital cost and operational complexity than high-temperature electrolysis (>700 °C). In this review, the latest advancements in low-temperature water electrolysers are provided from the classical membrane-based designs to new potential designs such as membrane-less designs. The coverage of electrodes by gas bubbles can cause a drastic loss in their activity and, hence, the hydrogen production efficiency of the device. To alleviate this issue, aerophobic and aerophilic electrodes are being developed. Their advantageous properties are discussed. Furthermore, models of water electrolysers are reviewed to provide critical understanding of the different parameters affecting the electrochemical performance of these devices. Finally, an industrial perspective is given to discuss the challenges in large-scale Gigawatt-level deployment of these devices in coming decades to meet future green hydrogen demand.

Broader impact

Excessive usage of fossil fuels in the last century to meet the energy demands of a rapidly growing population has caused global warming by drastically increasing CO_2 emissions. Hydrogen gas can play a key role in decarbonising the energy infrastructure. However, current hydrogen production is dominated by natural gas reforming and coal gasification, generating "grey" hydrogen with large CO_2 emissions. "Green" hydrogen with net-zero emissions could be produced through water electrolysis using renewable electricity, however, its high cost and low production efficiency are limiting its widespread utilisation. To meet the United Nations' climate goal of net-zero carbon emissions by 2050 (following the Paris Agreement), large-scale deployment of water electrolysers is required at the gigawatt level, which is a massive ramp-up from current deployment at the megawatt level. Several challenges, such as low current density, gas bubble accumulation and non-uniform water distribution exist in the electrolyser components (electrodes, gas diffusion layers and flow channels) of current cell designs. This review aims to provide a comprehensive overview of current and next-generation cell designs along with fundamental modelling studies of cell components to guide future designs that are more suitable for large-scale deployment at the industrial level.

1. Introduction

With rapid technological developments after the industrial revolution, urbanisation and population growth, demand for electricity has grown tremendously this past century, reaching ~33 000 TW h in 2024, which is expected to rise further by ~3% annually through 2026.[1] Fossil fuels, such as oil, natural gas or coal, have been the main source of energy for various sectors, however, their excessive usage has caused a significant increase of carbon dioxide emissions to the atmosphere, resulting in the greenhouse effect and global warming.[2] In this context, the

[a] *Centre for Nature Inspired Engineering & Department of Chemical Engineering, University College London, London, WC1E 7JE, UK. E-mail: p.trogadas@ucl.ac.uk, m.coppens@ucl.ac.uk*
[b] *TotalEnergies SE, OneTech, 2 Place Jean Millier, La Défense 6, 92078 Paris, France*
[c] *Institute of Chemistry and Chemical Engineering, Station 6, Ecole Polytechnique Fédérale de Lausanne, CH-1015 Lausanne, Switzerland*
[d] *Department of Chemistry, Aristotle University of Thessaloniki, 54124 Thessaloniki, Greece*

† Electronic supplementary information (ESI) available. See DOI: https://doi.org/10.1039/d4ee05559d

development of renewable alternatives with limited or no negative impact on the environment is necessary. The past decade has seen considerable efforts on a global scale with countries committing to achieve net zero emissions by 2050 (Paris Agreement 2015) *via* renewable energy technologies.[3,4] Among various options explored, hydrogen obtained *via* low carbon emission processes is a promising route towards decarbonisation.[5]

Hydrogen, traditionally used as chemical feedstock for, *e.g.*, ammonia production, is mainly produced by high carbon emissive processes, such as steam reforming of methane and gasification of coal or oil.[6,7] Interest has grown in pushing the research and development of hydrogen production by clean processes with limited or no CO_2 emission, such as the European Union (EU) 2020 ''Hydrogen Strategy for Climate-Neutral Europe'' and ''European Clean Hydrogen Alliance''.[8,9] Among several technologies, water electrolysis is a strong contender, since it utilises electricity to split water into hydrogen and oxygen.[10,11] Green production of hydrogen with net zero carbon emissions can be achieved through water electrolysis using electricity produced by renewable energy sources, such as wind or solar power.[12,13] Large-scale deployment of green hydrogen (also called renewable hydrogen) can mitigate the effects of climate change by decarbonisation of energy infrastructure and hard-to-abate sectors, such as aviation, shipping, steel, chemicals, and petrochemicals.[14] However, the current high cost of green hydrogen ($\sim$5 to 10 € per kg_{H_2})[15,16] limits its market share to only 4% of total hydrogen production and many other challenges, such as production efficiency, scalability and durability need to be addressed to increase its demand.[17] Amid the global hydrogen demand of $\sim$90 Mt in 2021, water electrolysers produce only a negligible amount ($\sim$40 kt) of green hydrogen.[6] The demand for renewable hydrogen is expected to grow drastically within the coming years and decades, requiring $\sim$100 Mt per year by 2030 and 500 Mt per year by 2050, according to the International Renewable Energy Agency (IRENA) to decarbonise carbon-intensive sectors.[18] The European Commission announced in its REPowerEU plan a projected domestic production of 10 Mt of renewable hydrogen in Europe by 2030, importing the same quantity from abroad.[19] The European Clean Hydrogen Alliance has set the target to install electrolysers at a Gigawatt-scale ($\sim$40 GW) by 2030 for green hydrogen production, a significant increase in its decarbonisation effort from the current installed capacity at a Megawatt-scale ($\sim$250 MW) in the EU.[9,20] To meet these ambitions, the global green hydrogen industry must be developed at a fast pace as IRENA's Transforming Energy Scenario for 2050 estimates deployment of electrolysers at the capacity of Terawatt-scale (at least 1.7 TW with further increase in case of deep decarbonisation scenarios).[18]

Water splitting ($H_2O \rightarrow H_2 + \frac{1}{2}O_2$) *via* electrolysis proceeds through two electrochemical reactions: the hydrogen evolution reaction (HER) at the cathode, involving a reduction reaction, and the oxygen evolution reaction (OER) at the anode, involving an oxidation reaction. These reactions follow different mechanisms in acidic and basic electrolytes.[21] Devices in which these electrochemical reactions take place are called electrolysers, which consist of electrodes coated with catalysts, a separator, bipolar plates, and flow channels. Low-temperature water electrolysis operating below 100 °C offers the advantages of a wide choice of compatible materials making operation simple, low-cost and durable, in contrast to high-temperature electrolysis, which offers better H_2 production efficiency but operates above 700 °C.[22,23] The current electrolyser technologies with their high cost of hydrogen production face several challenges at the cell level, *e.g.*, energy losses due to high overpotentials, bubble accumulation, inefficient catalyst utilisation, *etc.*[24–27] Therefore, novel electrolyser cell designs are urgently needed with improved efficiency, durability, cost competitiveness, and scalability to meet the rapid increase in demand for green hydrogen to achieve the net-zero targets of 2050.

This review presents the latest advancements of low-temperature electrolysers from current-generation, membrane-based (proton exchange or alkaline) electrolysers to the development of the next generation of electrolysers, using, for instance, a membrane-less design. Emphasis is given to various electrode designs for effective bubble management, as hydrogen and oxygen bubbles generated during the electrochemical reactions of water splitting cover the electrode surface, resulting in a drastic loss in hydrogen production efficiency of the device.[28–30] To further improve the design of these electrodes and accelerate their development, modelling should be used prior to their manufacturing, as it is a powerful tool that can reveal the relationship between their electrocatalytic as well as geometric characteristics and the efficiency of the device.[31] However, remarkably, there are only limited modelling reports in the literature on water electrolysers, indicating that this fundamentally guided approach is still at an early stage. Herein, a critical review of the reported models, either focusing on the electrode or the whole device, is presented to showcase the crucial parameters affecting the efficiency of water electrolysers and improve their design. An industrial perspective is added to discuss the potential and challenges in large Gigawatt-scale deployment of these devices needed to meet massive increase of green hydrogen demand in coming decades. We note that this perspective is missing in many papers, as most articles only discuss challenges at the lab scale, such as catalyst development.

2. Electrolyser technologies

2.1. Membrane-based designs

The current generation of industrial electrolysers utilise membranes to separate the produced hydrogen and oxygen gases from each other, which can form an explosive mixture (lower flammability limit: 4% of H_2 in O_2).[32,33] Various designs have been explored for these membrane-based water electrolysers, such as simple diaphragms for alkaline electrolysis,[34,35] proton exchange membranes (PEMs),[36,37] anion exchange membranes (AEMs),[38,39] and solid oxide ceramics.[40,41] PEM technology emerged in the 1960s during NASA's space programs, where lab-scale PEM cells provided high-purity hydrogen with compact designs.[42] Early laboratory versions struggled with membrane stability and high catalyst costs, limiting their industrial adaptation. Advances in these components

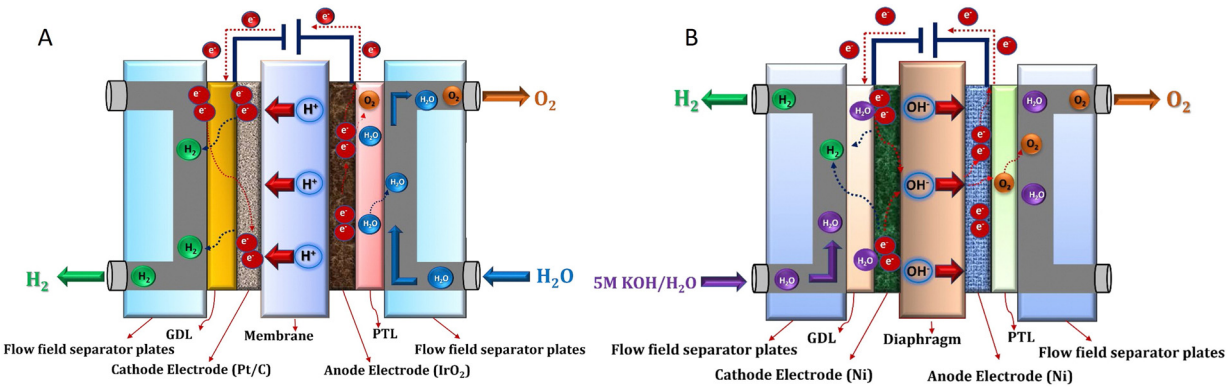

Fig. 1 Membrane-based electrolyser designs: (A) proton exchange membrane (PEM) and (B) alkaline exchange membrane (AEM). Reproduced with permission.[47] Copyright 2022, Elsevier.

(1980–2000) led to commercial PEM stacks (1–10 MW), which are now widely used in renewable green hydrogen projects.

A PEM electrolyser cell (Fig. 1A) comprises of two electrodes separated by a PEM (usually perfluorosulfonic acid, such as Nafion®) as a solid electrolyte in contrast to a liquid electrolyte present in an alkaline electrolyser. The most active catalysts for HER and OER reactions are platinum (Pt) and iridium oxide (IrO_2).[43–45] Therefore, two half-cell electrochemical reactions of the PEM electrolyser proceed on the catalytic materials, IrO_2 and Pt, which are coated on the anode and cathode, respectively.[46] A schematic diagram of different components of the PEM electrolyser is shown in Fig. 1A. Water is typically fed to the anode, producing oxygen, protons (H^+) and electrons (e^-) through an oxidation reaction (OER):

$$2H_2O \rightarrow O_2 + 4H^+ + 4e^- \quad (1)$$

It should be remembered that writing H^+, is just a simplified notation to describe a dynamic positively charged aqueous species, and not necessarily a lone proton. As electrons pass through the external circuit, protons selectively pass through the membrane and combine with electrons at the cathode to produce hydrogen through a reduction reaction (HER):

$$2H^+ + 2e^- \rightarrow 2H_2 \quad (2)$$

The main advantages of PEM electrolysers include high current density (>1 A cm^{-2}) and energy efficiency ($\sim$80%), production of hydrogen with high purity ($\geq$99.9%), as well as a robust design, even when powered by intermittent energy sources.[17] However, the utilisation of expensive and scarce noble metal catalysts remains a big challenge from a high ramping-up perspective.[48] Being a subproduct of platinum mining, the availability of iridium is limited, with an annual production of around 8–9 tons per year. Given that a 1 GW PEM plant would require between 5 to 10% of this iridium amount, large-scale industrial deployment seems very complicated to conceive. Therefore, novel electrodes with reduced metal loadings while maintaining high intrinsic catalytic activity are necessary for future large-scale deployment of PEM electrolysis.[49,50] Moreover, the degradation of fluorine-based membranes, potentially generating toxic polyfluoroalkyl substances (PFAS), remains a major topic to address.[51]

On the contrary, alkaline water electrolysis (AWE) is a mature, commercialised technology, which has been in use for almost a century.[6] Initially, AWE was utilised for industrial hydrogen production for use in fertiliser manufacturing (ammonia synthesis *via* the Haber–Bosch process) and petroleum refining.[42] Early systems used asbestos diaphragms and nickel electrodes, operating at low current densities. However, with improvements of these components and pressurised operation, it saw widespread adoption in the 1950s–1970s with MW-sized electrolysers, and, today, AWE remains dominant in large-scale hydrogen plants around the world.

An alkaline electrolyser cell (Fig. 1B) consists of two electrodes immersed in a liquid electrolyte (30–40% potassium hydroxide KOH). Water in a cathodic chamber undergoes an electrochemical reduction reaction on the electrode surface to form hydrogen and hydroxide (OH^-) ions:

$$2H_2O + 2e^- \rightarrow H_2 + 2OH^- \quad (3)$$

OH^- ions pass through a diaphragm to the anodic compartment and undergo an oxidation reaction at the electrode surface generating oxygen and water:

$$4OH^- \rightarrow O_2 + 2H_2O + 4e^- \quad (4)$$

The diaphragm generally consists of a porous zirconium oxide ceramic deposited on an open mesh polyphenylene sulfide fabric (Agfa's Zirfon®, 500 μm thick), whereas catalyst materials are classically RANEY® Ni and/or pure Ni mesh and potentially metallic alloys based on transition metal compounds, such as Ni, Co, Mn, and Fe oxides.[34] Alkaline electrolysers are less expensive than PEM (capital cost for a large >1 MW stack is $\sim$270$ per kW), due to the employed low-cost metals and electrocatalysts (Ni-based)[52] and can be easily scaled up (cell size $\sim$3 m^2) making them suitable for hydrogen production at industrial level.[17] However, alkaline electrolysers suffer from low current densities ($\sim$500 mA cm^{-2}), high energy consumption ($\sim$50–65 kW h per kg_{H_2}), corrosion of stainless steel elements of the balance of plant exposed to the alkaline electrolyte, and a long startup time, making them less suitable for use with intermittent electricity sources.[6,17,18]

2.2. New generation of designs

The major disadvantage of the design of electrolysers presented in the above section is the membrane itself, as it increases the electrical resistance and hence the cell overpotential ($\geq$0.2 V). The polymeric membrane undergoes irreversible degradation at high temperatures, resulting in a limited operating range (50–90 °C) and low voltage efficiency ($\sim$50–60%) of these electrolysers.[17] Hence, in recent years, various innovative new designs have been proposed, some of which are illustrated in Fig. 2.[53]

2.2.1. Flow-based membrane-less designs. The first membrane-less electrolyser employed a parallel flow field design with an inter-electrode distance of $\sim$105 μm.[58] This design leverages the Segré–Silberberg effect where neutrally buoyant gas bubbles assemble in an annulus, halfway between the centre of the electrolyser and the electrode, preventing the mixing of hydrogen and oxygen in the main chamber.[53] As a result, a low $\sim$0.4% gas crossover is achieved using platinum electrodes at $\sim$300 mA cm^{-2} and 2.6 V with 42% energy efficiency.[58]

Mesh flow-through electrodes employing RuO_2/IrO_2 and Pt as anode and cathode, respectively, with a $\sim$0.8 mm gap interelectrode distance and electrolyte velocity $>$0.1 m s^{-1} cause the formation of gas bubbles on the surface of the electrodes, which then move through their porous structure towards the back chamber.[59] As a result, high-purity hydrogen ($\sim$99.83%) is generated, while operating at a current density of $\sim$3500 mA cm^{-2}. A similar design to the above exhibits similar results, in which the mesh electrodes (Fig. 2B) are placed at an angle instead of parallel to each other.[55] This architecture allows the flow of acidic or alkaline electrolyte into two separate effluent channels where the produced gases are separated from each other by a thin barrier. Electrolyser operation with $\sim$72.5% efficiency and $\sim$2.8% H_2 crossover is achieved at $\sim$100 mA cm^{-2} and $\sim$26.5 cm s^{-1} fluid flow.[55] This Y-shaped cell design demonstrates improved gas separation and uniform current distribution compared to conventional I- and T-shaped membrane-less designs. Stable operation at a current density up to 250 mA cm^{-2} is achieved with an efficient bubble removal rate from the surface of the electrode.[60]

Another successful design of a membrane-less electrolyser relies on permeable solid barriers to keep produced gas bubbles separate instead of leveraging the Segré–Silberberg effect.[56] It comprises three separate channels where the electrolyte is introduced into the central channel and subsequently diffuses into the outer channels through the porous walls

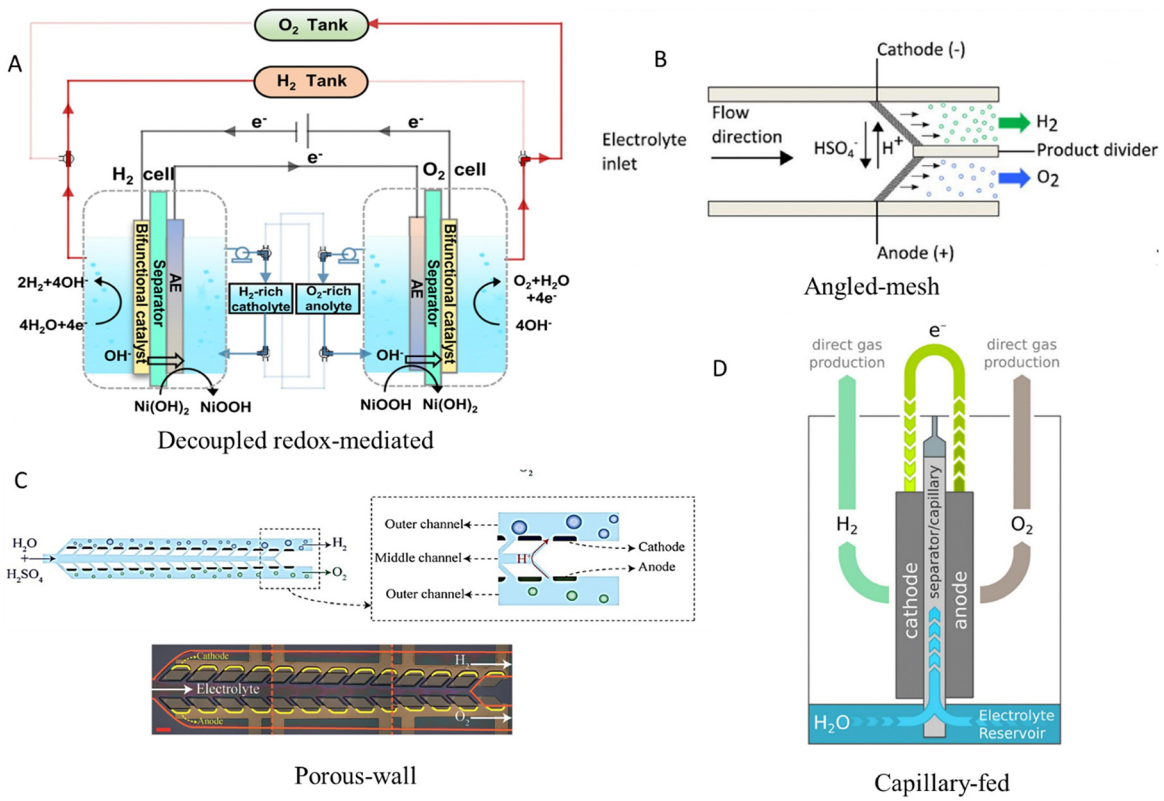

Fig. 2 Membrane-less electrolyser designs. (A) Decoupled electrolysis operation of oxygen and hydrogen evolution in two separate compartments mediated by an auxiliary electrode (AE) coated with a redox couple of NiOOH/$Ni(OH)_2$ electrocatalyst. Reproduced with permission.[54] Copyright 2021, Springer Nature. (B) 3D printed porous electrodes placed at an angle to each other, enabling product gases to accumulate in separate channels. Reproduced with permission.[55] Copyright 2016, The Electrochemical Society and IOP Publishing. (C) Microfluidic porous wall electrolyser, utilising permeable solid barriers instead of fluidic forces to keep gases separate. Reproduced with permission.[56] Copyright 2021, The Royal Society of Chemistry. (D) Capillary-fed operation where electrodes receive a continuous flow of electrolyte through natural capillary action within an intermediate separator whose lower end is immersed in an electrolyte. Reproduced with permission.[57] Copyright 2022, Springer Nature.

(Fig. 2C). Electrodes are positioned on the exterior of these porous walls. As a result, product gas bubbles of hydrogen and oxygen are formed only in the separate outer channels and do not enter the central channel, as the continuous flow of the electrolyte prevents them from mixing. This results in a very low gas crossover of ~0.14% at ~300 mA cm^{-2} and electrolyte flowrate of ~80 ml h^{-1} which is ~58 times lower than the gas crossover for a membrane-less electrolyser with electrodes parallel to each other under similar operating conditions.[56] Electrolyser scaling is possible without increasing interelectrode distance due to the absence of bubble flow, even though the fabrication of inclined pores as well as selective catalyst deposition remains challenging, whereas additive manufacturing can potentially provide some solution to these issues with the customisation of the porous network of the electrode.

2.2.2. Decoupled electrolysis-based membrane-less designs. A large interelectrode distance in membrane-less electrolysers causes Ohmic losses, resulting in lower current density and high operating voltage (>2.5 V). This issue is resolved *via* the decoupled electrolysis operation of oxygen and hydrogen evolution in two separate compartments only connected through a wire to transfer electrons (Fig. 2A).[54] Each compartment has a sandwich-type design containing a working electrode coated with bifunctional catalyst (FeP–CoP over nitrogen-doped carbon), a porous separator and an auxiliary electrode (AE); a counter electrode is also included in the setup to complete the circuit and allow current to flow. The AE is coated with a redox couple of $NiOOH/Ni(OH)_2$ with a continuous flow of anolyte and catholyte in each compartment. With low Ohmic resistance due to the shorter distance for ions to travel in this compact design, it achieves a high current density of ~750 mA cm^{-2} at 2.1 V (*vs.* reversible hydrogen electrode (RHE)), which is comparable to the current density generated by a PEM electrolyser.[17] Furthermore, continuous cyclic operation is achieved by switching the electric polarity of the cell, typically occurring every 10 min. when AE materials are nearly all converted from $Ni(OH)_2$ to NiOOH in the case of HER and *vice versa* for the OER at the end of each cycle. In the presence of two resistive counter electrodes, some energy loss occurs, which is minimised by compact cell design, resulting in a faradaic efficiency of ~96.5%. Continuous cycling limits catalyst choices as it requires bifunctional catalysts for both OER and HER.[54] A decoupled water electrolysis system has been developed utilising a tri-functional electrode, graphite felt-supported nickel–cobalt phosphate ($GF@Ni_1Co_1$–P) working as a redox mediator, HER catalyst, and OER catalyst.[61] This decoupled system operates at a total voltage of 1.68 V at 5 mA, with faradaic efficiencies of 98.4% for H_2 and 94.5% for O_2 production and maintains stable operation over 400 cycles.[61]

2.2.3. Capillary-fed membrane-based design. In the capillary-fed electrolyser, the lower end of a separator is immersed in liquid water and the upper part is sandwiched between two gas diffusion electrodes, which draw liquid laterally, covering their surface with a thin layer of electrolyte.[57] NiFeOOH and Pt/C are used as the anode and cathode, respectively, in contact with a continuous flow of aqueous electrolyte *via* capillary action occurring in the hydrophilic separator situated between these electrodes (Fig. 2D). Application of a voltage results in the generation of oxygen and hydrogen in separate gas chambers, resulting in bubble-free operation at the electrodes. This innovative design results in superior electrochemical performance (~40.4 kW h energy usage per kg_{H_2}) with alkaline electrolyte compared to commercial electrolytic cells (~47.5 kW h power consumption per kg_{H_2}) and achieving a high current density of ~500 mA cm^{-2} at only ~1.51 V with 98% efficiency at the cell level. When integrated into bipolar stacks with 500 individual cells, it showed performance comparable to conventional PEM and alkaline stacks.[57] At the system level with stack and balance of plant included, it demonstrated 95% efficiency (~41.5 kW h per kg_{H_2}) compared with conventional electrolysers having 75% efficiency (~52.5 kW h per kg_{H_2}).[62]

3. Electrodes and bubble management for water electrolysis

The electrodes are key components of a water electrolyser. Their design significantly influences the H_2 production efficiency.[48,63,64] The choice of electrocatalyst in the electrode plays a crucial role in determining the electrochemical performance of the cell, which is often dependent on its nanostructure and material type. High current density in HER and OER electrochemical reactions is often achieved by either increasing the intrinsic activity of the catalyst or the number of its active sites.[65] Various strategies are utilised for the synthesis of highly efficient electrocatalysts, including alloying,[66–68] doping,[69,70] morphology engineering,[71,72] porous nano-structuring,[73,74] loading on high surface area supports,[49,75,76] and reducing the particle size to ultra-small,[77,78] or single atoms.[74,79] Several recent reviews[80–85] discuss in detail the design of the electrocatalysts for water splitting reactions and aspects of electrode engineering[48,63,86,87] for current generation membrane-based electrolysers. Interested readers are referred to these articles for further information. As redox reactions of water splitting occur on the electrocatalysts coated on these electrodes, hydrogen and oxygen bubbles are generated from product gases. When these bubbles cover the electrode surface this results in lower production efficiency of the device due to an increase of activation and Ohmic overpotentials.[88,89] These bubbles-induced overpotentials for water electrolysis are substantial, ranging from ~80 mV at 10 mA cm^{-2} in the case of nanobubbles to ~308 mV at above 500 mA cm^{-2}.[28] The development of novel electrodes for effective bubble management is crucial for next-generation devices, *e.g.*, in membrane-less designs, where product gases could mix, posing a safety risk.[90–92]

Bubble coverage on gas-evolving electrodes generally increases with current density, whereas an increase of temperature and pressure decreases it.[93] Bubble break-off radius (R_r) and volume (V_r) immediately prior to its detachment can also impact the amount of electrode bubble coverage.[93] Moreover, higher flow velocity in electrolyser microchannels is favourable, as it reduces bubble detachment diameter and time.[94]

Electrocatalytic gas evolution is governed by the Marangoni effect, which refers to a flow driven by variations in surface

tension along the gas–liquid interface caused by temperature (thermo-capillary force) or concentration gradients (solute-capillary flow).[95–97] The non-uniform coverage of the electrode by gas bubbles produced during the electrochemical reactions results in the appearance of a solutal Marangoni force.[98] Such force causes the gas bubbles to oscillate along the surface of the electrode, leading to a self-pinning effect preventing the gas bubbles from leaving the surface. When instead, these bubbles are relocated to the bubble-free side of the electrode, it exposes the previously covered electrode surface to ensure the production and growth of gas bubbles.[96] The understanding of Marangoni effects on gas bubble dynamics at the nanoscale remains elusive, due to the limitations in current technology, which cannot provide detailed information on the morphology and growth of gas bubbles.[99] These limitations could be overcome *via* molecular dynamics simulations,[96] or dark field microscopy[100] providing valuable insights on the nucleation and growth of nanobubbles.

Bubbles covering the electrode are typically micrometre sized (10–800 μm) during continuous water electrolysis.[101,102] Transient nanobubbles, which appear for a very short time (1–100 μs) as a result of gas supersaturation, dissolve rapidly in electrolyte during water electrolysis.[103] However, highly stable surface nanobubbles on an electrode are observed by atomic force microscopy.[104] These nanobubbles, characterised by long lifetime and low contact angle, require location gas supersaturation and contact line pinning for their stability.[105] Moreover, molecular dynamic simulations of single electrolytic nanobubbles reveal that a threshold current density (or a threshold gas flux ~10–12 kg m^{-2} s^{-1}) exists. Below this threshold, the nanobubbles are stable, whereas the nanobubbles grow indefinitely and detach from the surface of the electrode by buoyancy for a gas flux higher than its threshold value.[106]

Bubble management in water electrolysers can be achieved by electrode surface engineering or alteration of the operating conditions, such as pressure or electrolyte composition.[28,107] Superwetting electrodes with superaerophobic or superaerophilic properties have gathered significant attention for electrochemical reactions involving gases.[108] The next section discusses various superwetting electrode designs utilised for effective bubble management.

3.1. Aerophobic electrodes

Morphology tuning and chemical surface modification of electrodes have been explored in the literature to make them bubble-repellent and achieve better electrochemical performance in water electrolysis.[109–111] Nano-structuring the catalyst layer to make a porous electrode can improve its surface utilisation as well as multiphase transport.[65,112] For example, honeycomb (HC) nanostructured electrodes have unique porous morphology and high surface area, which provides efficient ion transport, improved conductivity and mechanical stability.[113] An HC-structured iridium (Ir) catalyst layer (Fig. 3A) has a large electrochemically active surface area (outer charge Q ~71.4 mC cm^{-2} for HC Ir and ~32.9 mC cm^{-2} for dense Ir, respectively) with much lower Ir loading of ~0.27 mg cm^{-2} on the anode (compared to 3 mg cm^{-2} for typical anode catalyst).[101] As a result, a ~2.2 times improvement in OER performance is achieved compared to a dense Ir-coated electrode due to its higher mass activity of 4.16 A mg^{-1}. The HC design favours the formation of smaller bubbles (~100 μm) with the majority of bubbles detaching within the 10–20 μm range and it achieves a low cell voltage of 1.8 V at 2 A cm^{-2} current density in electrolyser operation.[101] Instead of Ir, a nickel/gold (Ni/Au) honeycomb structured electrode, prepared *via* hard templating employing ~100–300 nm polystyrene beads, is a feasible alternative.[114] Compared to a flat Ni/Au electrode,

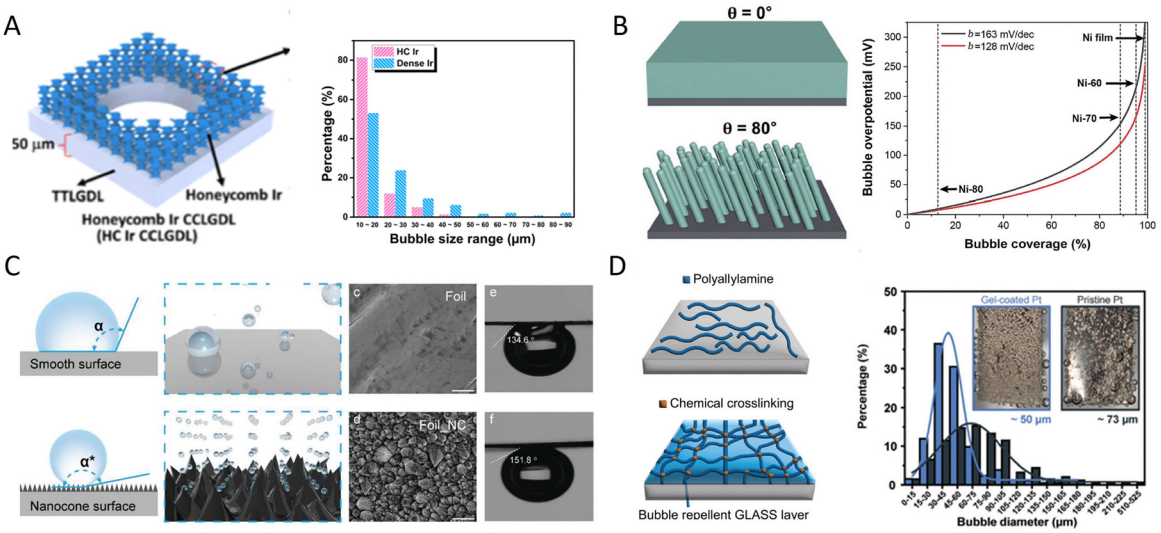

Fig. 3 Aerophobic electrode designs: (A) honeycomb structured Ir catalyst layer. Reproduced with permission.[101] Copyright 2023, American Chemical Society. (B) Oblique angles deposited nickel nanorod arrays-based Ni films. Reproduced with permission.[115] Copyright 2023, Wiley-VCH. (C) Electrodeposited nickel nanocones-based Ni electrodes. Reproduced with permission.[116] Copyright 2023, Wiley-VCH. (D) Bubble-repellent fibrous polyallylamine hydrogels coated Pt/Ni foils. Reproduced with permission.[102] Copyright 2023, Wiley-VCH.

much improved HER activity with 115 mV reduction of overpotential is observed for a HC Ni/Au electrode containing a uniform distribution of holes with ~31 nm diameter.[114] This is attributed to the change in surface wettability as the average bubble diameter decreases from ~519 μm for a flat Ni/Au electrode to ~128 μm for this modified electrode.

Depositing nanomaterials on the surface of the electrocatalyst can alter its wetting properties for favourable bubble detachment by reducing their contact area and adhesion. To elucidate the effect of surface morphology of catalyst thin films, nickel nanorod arrays have been deposited at oblique angles from 60 to 80° on a flat Ni-film (Fig. 3B) using an electron beam evaporator.[115] Ni arrays deposited at 80° angle (Ni-80) have the highest porosity of 52% and an air contact angle of 156°. As a result, Ni-80 produced an ~2.4 times smaller bubble radius and released bubbles ~3.8 times faster than a flat Ni-film, resulting in much reduced overpotentials at a current density of 100 mA cm^{-2} for HER. Further investigation by chronopotentiometry reveals a nearly mass transfer-free reaction for Ni-80, as the potential remained stable from 100 to 1600 RPM, whereas noticeable fluctuations in voltage are seen for a flat Ni-film below 400 RPM.[115] Nickel nanocones (NC) with base sizes ranging from 300 to 700 nm have been electrodeposited on various types of nickel electrodes (foil, foam and 3D printed lattices) to increase their aerophobicity, retaining >95% of electrolyser performance over 100 h of operation at ~900 mA cm^{-2} (Fig. 3C).[116] Visualisation of hundreds of bubbles generated at different locations on the electrode, *via* high-speed camera measurements, confirms the smaller size of the bubbles (~97 μm *vs.* ~379 μm) and their shorter residence time (~3 s *vs.* ~56 s) on NC-modified electrodes compared to pristine nickel foil for both HER and OER. This is because the adhesion force exerted on bubbles by a NC-modified electrode surface creates an angle instead of being perpendicular to the flat electrode surface, thereby reducing its effect on the opposite, upward buoyancy force on bubbles and promoting their easier detachment.[116] Transition metal layered double hydroxide (LDH) has been deposited on a Ni foam (NF) electrode by hydrothermal treatment with metal precursors for 12 h.[117] This results in the vertical growth of hierarchical nanoarrays with 2D nanosheets (~58–105 nm thickness) and 1D nanowires (~1.7 μm length), intersecting at 75° angle and forming a knitted structured surface with superaerophobicity (contact angle (CA) ~151°). This modified electrode exhibits excellent OER performance in alkaline seawater with a low overpotential of ~320 mV at 400 mA cm^{-2}, and negligible reduction (~19 mV) in overpotential occurs after 300 h of operation at 100 mA cm^{-2}.[117]

Apart from surface structural engineering to create an aerophobic electrode, chemical coating of the surface can also modulate the bubble adhesion force to facilitate its early detachment.[102,111,118] Layer-by-layer deposition is employed on a NF electrode by conjugate reaction between acrylate and amine groups of polymeric chemical modifiers to achieve a very low adhesion force of ~4.6 μN for H_2 bubbles.[111] Apart from superior HER activity at a high current density of 500 mA cm^{-2} with ~512 mV overpotential compared to ~748 mV for bare NF electrode, it also shows low overpotential (~250 mV) at a lower current density of 100 mA cm^{-2} where smaller gas bubbles tend to attach more firmly to the unmodified electrode due to smaller buoyancy forces. Physical coating of the catalyst surface also provides an alternative route to fabricate aerophobic surfaces with lower cost and easy scale-up.[102,118] Large area superaerophobic electrodes up to 100 cm^2 in size can be fabricated by spin coating of fibrous polyallylamine hydrogels on Pt-coated Ni foils (Fig. 3D).[102] The porous network of this hydrogel provides removal pathways for bubbles resulting in better HER and OER activity in a three-electrode system and an improved polarisation curve in a two-electrode cell compared to a pristine Pt electrode. Polyethylenimine (PEI) hydrogel coating on platinum-coated FTO and NF electrodes has also been deposited *via* condensation reaction of precursors and freeze-drying.[118] Hydrogels with optimum 2 wt% PEI concentration have the highest porosity of ~10.94% with an average pore size of ~20.18 μm creating a superaerophobic electrode surface with an air contact angle above 150°. As a result, lower HER overpotential (~608 mV *vs.* ~774 mV of bare NF electrode) at 500 mA cm^{-2} and stable voltage for 20 h of operation in an alkaline medium is achieved.

Superaerophobic designs can effectively remove bubbles from an electrode surface in membrane-based electrolysers and enhance their electrochemical performance. To implement such technical solutions in industrially relevant systems, the challenge remains of transferring such preparation methods to large-scale production. Furthermore, in the case of the development of membrane-less electrolysers, such superaerophobic design may not be a suitable choice, as hydrogen and oxygen gas bubbles repelled from the electrode surfaces can then mix in the main chamber. Hence, there are no literature reports so far on using superaerophobic electrodes in membrane-less electrolysers. However, the modification of the surface of the electrode to moderate bubble adhesion *via* alteration of its orientation has been utilised to increase the efficiency of a membrane-less water electrolyser.[90] This tilted micro-cone array (TMCA) electrode fabricated by electrochemical etching of Cu foil with an optimised tilting angle of 50° provides facile, unidirectional bubble transport, preventing bubble accumulation and gas crossover. At a current density of 240 mA cm^{-2}, the TMCA electrode achieves 99.99% pure hydrogen separation with an interelectrode distance of just 1.5 mm, compared to conventional designs with superaerophobic electrodes, which only achieve 88.3% H_2 purity.[90] This issue of gas mixing in membraneless electrolysers can be resolved using aerophilic electrodes, providing an effective strategy for bubble management and prevention of gas crossover for these electrolysers.[119]

3.2. Aerophilic electrodes

Aerophilic electrodes have been explored for directional bubble transportation by utilising a hydrophobic membrane coating or structural modifications of electrodes.[91,120] A breathable anode electrode (Fig. 4A) has been prepared by sputter deposition of ~30–40 nm sized platinum nanoparticles on hydrophobic

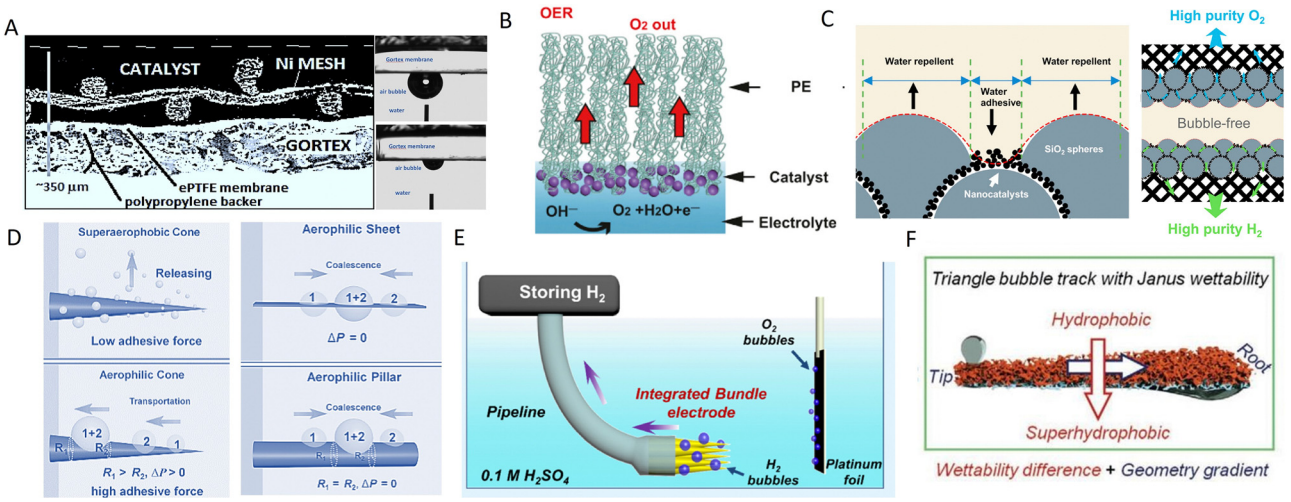

Fig. 4 Aerophilic electrode designs (A) Porous electrode prepared by coating Ni-based catalysts on hydrophobic PTFE membrane. Reproduced with permission.[91] Copyright 2019, Elsevier. (B) Alveolus-like oxygen electrode with Au/$NiFeO_x$ catalyst layer of 50–100 nm thickness on hydrophobic nanoporous polyethylene substrate. Reproduced with permission.[121] Copyright 2018, Elsevier. (C) Rose-petal-effect mimicking electrode. Reproduced with permission.[92] Copyright 2023, Elsevier. (D) Hydrophobic cone electrode by electroetching of copper wire and silica nanoparticle coating. Reproduced with permission.[122] Copyright 2016, Wiley-VCH. (E) Integrated copper cones array electrode with wettability gradient due to concentration variation of aerophilic silica nanoparticle from tip to base. Reproduced with permission.[123] Copyright 2021, American Chemical Society. (F) Conical nickel foam electrode with asymmetric wettability for dual self-propelled bubble transport. Reproduced with permission.[124] Copyright 2020, Wiley-VCH.

polytetrafluoroethylene (PTFE) membrane (Gore-Tex), with well-defined pores and narrow size distribution of 1–10 μm.[119] This electrode rapidly removes oxygen bubbles (~92%) from its surface, reducing the need for a separator to prevent gas cross-over. Another porous electrode is fabricated by incorporating an inactive hydrophobic layer of polyethylene on the catalyst layer to direct formed bubbles to the gas chamber at the back of the electrode.[91] This concept enables the fabrication of a bubble-less alkaline electrolyser using $NiCo_2O_4$ and Ni as anode and cathode catalysts, respectively, without any membrane between electrodes. It achieves a very low onset potential of ~1.28 V due to the significantly reduced electrode overpotentials (~0.11 V at anode) at 10 mA cm^{-2}.

Apart from utilising hydrophobic membranes for bubble removal from the surface of the electrodes in water electrolysers, nanostructured electrodes with geometry gradients are also explored as an alternative for effective bubble removal.[122,123] A hydrophobic cone-shaped electrode (Fig. 4D) is fabricated by electroetching of a copper wire (~0.8 mm diameter) and immersion in 1-dodecanethiol solution for 12 h.[122] Its conical structure creates a Laplace pressure difference for gas bubbles, which, coupled with the hydrophobic surface (contact angle ~102.3°) and high adhesive force of ~167 μN, results in efficient movement of bubbles from the tip to the base of the electrode in the HER reaction. The wettability of this hydrophobic cone-shaped electrode can be further improved by coating superhydrophobic nano-silica particles. This enables the facile transportation of produced hydrogen during HER at the base of an integrated bundle electrode consisting of an array of copper cones (Fig. 4E) and its continuous removal from the reaction chamber.[123] Combined concepts of geometry gradient and wettability difference, seen in Janus materials with opposite wetting properties,[125,126] can be used to design an electrode with dual self-propelled bubble transport interface, enabling more efficient bubble removal. Such an example is a Janus nickel foam electrode (Fig. 4F), consisting of a hydrophobic (CA ~ 125°) and superhydrophobic (CA ~ 158°) surface on opposite sides of its hierarchical structure, resulting in the directional self-transport of generated gas bubbles.[124]

Study of gas bubble manipulation by biological organisms found in nature (such as, super-aerophilic lotus leaf, super-aerophobic fish scale, or asymmetric pitcher plant peristome) has provided an effective strategy to address gas bubble issues of electrochemical reactions.[127] The mammalian lung is one of the most efficient gas exchange systems in nature for breathing. It utilises tiny sacs called alveoli at the end of bronchioli for two-way gas diffusion.[128] Air inhaled into lungs and CO_2 in blood capillaries are exchanged through a micron-thick alveolus membrane, whose asymmetric wetting properties facilitate rapid gas diffusion. Inspired by this sophisticated design, an alveolus-imitating oxygen electrode has been fabricated, mimicking the breathing mechanism of mammals by coating an Au/$NiFeO_x$ catalyst layer of ~50–100 nm thickness on a nanoporous polyethylene (PE) membrane of 12 μm thickness.[121] O_2 molecules formed on the hydrophilic catalyst surface undergo rapid diffusion into the gas phase through the hydrophobic PE membrane, which is impenetrable for water. This electrode achieves a low onset potential of 1.42 V (*vs.* RHE) at 10 mA cm^{-2} in the alkaline OER with bubble-free operation due to a reduced overpotential to only 0.19 V. A rose petal surface displays a wetting regime with high water contact angle, which prevents a water droplet from leaving its surface, unlike a lotus leaf, where a water droplet rolls over and leaves the surface.[129] This originates from multiscale surface roughness with alternate blocks of superhydrophobic (nanoscale folds on micro papillae) and water adhesive (grooves

between micro papillae) patches. As these features are useful for efficient contact of electrolyte and catalyst to minimise overpotentials and remove gas quickly, an electrode design was proposed (Fig. 4C) for bubble-less electrolysis imitating the rose petal effect having multiscale roughness with adhesive superhydrophobicity ($\sim$161°).[92] Alternate water adhesion and repelling blocks are created by filling hydrophilic Pt/C nanoparticles to the void spaces of closely packed hydrophobic silica (SiO_2) microspheres through mixing and loading on carbon paper substrate. This allows the quick release of formed bubbles by spreading and moving away from the catalyst surface compared to a conventional aerophilic electrode,[119] where gas bubbles need to diffuse through the membrane electrode assembly (MEA) of high diffusion resistance for their removal. As a result, a high current density of $\sim$4.2 A cm^{-2} is achieved for this rose petal mimetic electrode in bubble-less HER reaction with $\sim$61.5% H_2 production efficiency and negligible gas crossover ($\sim$0.003% at 1 mm interelectrode distance) occurs for membrane-less electrolyser operation.[92]

Instead of designing an electrode with bubble repelling or attracting property alone, electrodes with localised aerophobic and aerophilic patches have been designed for directional movement and removal of gas bubbles.[130–133] A novel electrode incorporating a pattern of stripes of superaerophobic (SAB) electrocatalytic Pt and superaerophilic (SAL) SiO_2 nanoparticles (Fig. 5A) has been fabricated for HER.[132] As H_2 bubbles are formed on a Pt surface in the SAB stripe with an optimal width of 250 μm, they are quickly moved into adjacent regions of SAL stripes with an optimal width of 500 μm, working as gas channels transporting hydrogen out of the reaction system. This design keeps the electrocatalyst surface clean from any blockage by bubble adhesion and enhances the H^+ diffusion from the bulk acid electrolyte. Finite element simulations reveal that the H_2 concentration at the electrode reduced from 0.66 M to 0.29 M by the introduction of adjacent SAL stripes, which reduce the H_2 diffusion distance owing to the presence of a gas cushion, resulting in much reduced overpotentials of −80 mV compared to −511 mV for a flat Pt electrode.[132] Another electrode design (Fig. 5B) employs microporous stainless-steel mesh (1 × 1 cm), which is spray-coated with PTFE on one side and contains the Pt/C electrocatalyst on the other side.[133] This enables directional bubble movement from the aerophobic catalyst side to the aerophobic PTFE side through the pores of a mesh, leading to a $\sim$15 times enhancement of HER current density.

In summary, electrode wettability in water electrolysis is dynamic, influenced by surface properties, applied potential, and gas evolution. When a voltage is applied, the distribution of ions at the electrode–electrolyte interface changes, causing a shift in surface charge. This phenomenon, known as the electrocapillary effect,[134] can modify the wettability of the electrode, while gas films increase local hydrophobicity, hindering electrolyte contact. To counter this, nanostructuring, coatings, and chemical treatments enhance wetting,[102,111,114,115] while surfactants and pH

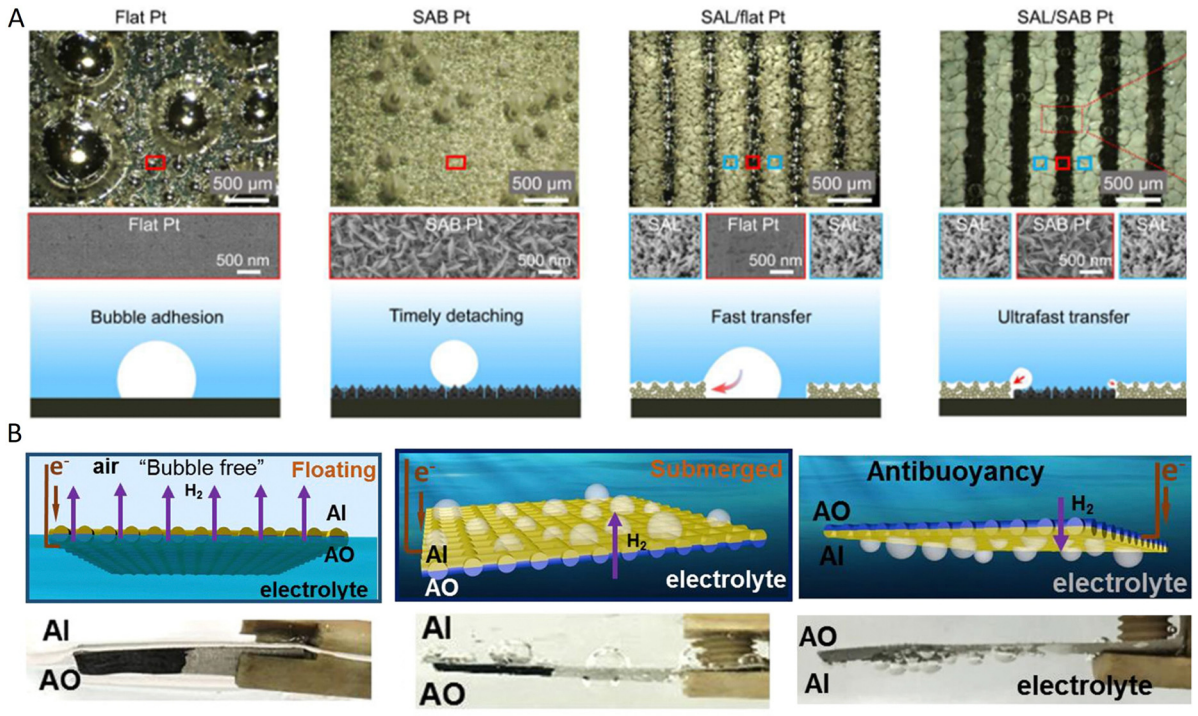

Fig. 5 Electrode designs with aerophilic/aerophobic patches for directional removal of bubbles: (A) electrode with alternative stripes of micrometre width of superaerophobic (SAB) electrocatalytic Pt and superaerophilic (SAL) SiO_2 nanoparticles for HER reaction. Reproduced with permission.[132] Copyright 2023, American Association for the Advancement of Science. (B) stainless-steel mesh electrode, with aerophilic (Al) coating of polytetrafluoroethylene (PTFE) on one side and aerophobic (AO) Pt/C catalyst on the other side. Reproduced with permission.[133] Copyright 2020, American Chemical Society.

adjustments can optimise electrode-liquid interactions.[135–137] To ensure efficient gas removal and maintain electrode wettability, understanding these factors is essential for the optimised electrochemical performance of water electrolysers.

4. Electrolyser models

For the development of advanced water electrolysis devices, data are often needed under various operating conditions and using various materials.[21,138,139] Modelling of water electrolysers can aid towards this goal, since it is a powerful tool for understanding the relationship between structure/property and electrochemical performance, which can accelerate the technology development by saving time and cost of experiments.[31] Electrolyser models can be grouped into two categories: the first one investigates the integral behaviour of the complete cell (*e.g.* polarisation curve) as a function of the operating conditions, while the second category focuses on individual functional layers of the electrolyser device (electrode, gas diffusion layer (GDL), flow field) to obtain a mechanistic understanding of the underlying phenomena (*e.g.* gas and water transport).[140]

Most of the electrolyser models utilise a continuum approach, which applies principles of classical fluid dynamics and electrochemistry, treating the electrode, GDL and electrolyte as continuous media.[141,142] With the advancement of computational power and the realisation that the microstructure of the electrode and the GDL significantly impact transport phenomena, pore-scale models have been developed recently for electrolysers.[143,144] With the development of artificial intelligence in the past decade, machine learning based predictive models are developed as well, which can analyse much larger and more complex datasets with high accuracy. These tools could accelerate the development and optimisation of key components of water electrolysers, such as electrocatalysts and the membrane electrode assembly (MEA).[145,146]

Models developed thus far for water electrolysers face several challenges, such as computational resources, complexity, data requirements, and validation.[31] However, literature on modelling water electrolysers is scant,[147–149] and a review summarising the state-of-the-art and problems in model development is lacking. Therefore, a comprehensive overview of models with various levels of detail (complete cell models to layer-specific models) is provided here, that can serve as a tool for their further advancement.

4.1. Layer specific models

4.1.1. Electrode models. As the electrode is an important component of the electrolyser, where an electrochemical reaction takes place converting water to hydrogen and oxygen, there is a need to model it to optimise its design.[150] The dependence between the electrode potential and the concentration of the species involved in any electrochemical reaction is dictated by the Nernst equation:[151]

$$E = E^0 + \frac{RT}{nF}\ln\left(\frac{a_0^*}{a_R^*}\right) \quad (5)$$

where E^0 is the standard electrode potential (V) *vs.* standard hydrogen electrode (SHE), a^* is the bulk activity for the considered species (oxidised or reduced) (mol cm^{-3}), F is Faraday constant (C mol^{-1}), R is the universal gas constant (J K^{-1} mol^{-1}), and n is the number of electrons involved. Mass transfer on the electrode surface is dictated by the Nernst–Planck equation:[152]

$$N_i(x) = C_i v(x) - D_i\frac{dC_i(x)}{dx} - \frac{z_i F}{RT}D_i C_i\frac{d\phi_i(x)}{dx} \quad (6)$$

Each term on the right-hand side of eqn (6) represents convection, diffusion (concentration gradient) and migration contributions, respectively, where $N_i(x)$ is the flux of species i (mol s^{-1} cm^{-2}) at a distance x (cm) from the electrode surface, D_i is the diffusion coefficient (cm^2 s^{-1}), z_i *is* the charge (unitless), C_i is the concentration (mol cm^{-3}), $v(x)$ is the velocity (cm s^{-1}) with which a volume element in solution moves along the axis, $\frac{dC_i(x)}{dx}$ is the concentration gradient and $\frac{d\phi_i(x)}{dx}$ is the potential gradient at distance x, neglecting any pressure or temperature gradient, and electro-osmosis.

Several equations have been developed to capture the kinetics of electrochemical reactions at the electrolyte-electrode interface, the most notable of which is the Butler–Volmer equation, which computes electrode current density i as a function of the activation overpotential η:[152]

$$i = i_0\left[\exp\left(\frac{\alpha_a F\eta}{RT}\right) - \exp\left(\frac{-\alpha_c F\eta}{RT}\right)\right] \quad (7)$$

where α_c and α_a are the cathodic and anodic charge transfer coefficients (unitless), respectively, i_0 is the exchange current density (A cm^{-2}), and η is the overpotential (V).

At higher overpotentials (>50 mV), the Tafel equation can be used to describe electrode kinetics, which links applied overpotential η to the current i passing through the electrode:[152]

$$\eta = \pm\left(\frac{RT}{\alpha F}\ln i_0 - \frac{RT}{\alpha F}\ln i\right) \quad (8)$$

where i_0 is the exchange current (A). A simplified form of this equation is often used:

$$\eta = a + b \times \ln i \quad (9)$$

where a and b are constants which can be calculated by plotting η *vs.* $\ln i$, also known as the Tafel plot, providing important information about the electrochemical activity of an electrode for a specific reaction.[153]

Modelling of the gas bubbles formed during electrochemical reactions in an electrolyser is of significant interest, as their coverage of the electrode surface has a detrimental effect on cell overpotential.[154] Gas bubbles undergo nucleation first on the electrode surface, after which their growth and detachment take place.[155] The geometry of the electrode surface and its wettability are the two most influential parameters affecting the gas bubble behaviour. Hence, the tuning of these properties provides an important strategy for effective bubble management and improved electrochemical performance.[150,156]

Bubbles formed in water electrolysis are modelled using Lagrangian or Eulerian approaches.[155,157] The Lagrangian approach allows the monitoring of individual gas bubbles at the gas–liquid interface.[155] For example, a gas–liquid two-phase model is developed to simulate the flow, as well as the growth and detachment of gas bubbles from the surface of the electrode (Fig. 6A).[156] The model provides detailed information on bubble detachment and coalescence from the electrode surface and in bulk electrolyte, considering the wettability of the electrode surface as well as the size of the bubbles, *via* Cahn–Hilliard (C–H) eqn (10) and (11):

$$\frac{\partial \phi}{\partial t} + \vec{u} \cdot \nabla \phi = \nabla \cdot \left(\frac{\gamma \lambda}{\varepsilon_{pf}^2} \nabla \psi \right) \quad (10)$$

$$\psi = -\nabla \cdot (\varepsilon_{pf}^2 \nabla \phi) - (\phi^2 - 1)\phi \quad (11)$$

where ϕ is the phase-field parameter ($\phi = -1$ for fluid 1, $\phi = 1$ for fluid 2 and $\phi = 0$ for the interface), ψ is the free energy (J m^{-3}), ε_{pf} is the interfacial thickness (m), $\vec{u}$ is the velocity field (m s^{-1}), γ is the mobility (m^3 s kg^{-1}) and λ is the mixing energy density (N). It is revealed that the coalescence of smaller bubbles on the surface of the electrode is the main mechanism for the detachment of gas bubbles.[156] The hydrophilic surface of the electrode with a sufficiently small contact angle ($\sim \pi/5$) shrinks bubbles to a round shape that are less attached to the solid surface. Further decrease of the contact angle detaches and repels this round bubble from the surface of the electrode into the bulk electrolyte. The smaller the contact angle (from $\pi/5$ to $\pi/9$) of the bubble, the further the bubble is repelled.[156]

In another Lagrangian model, the growth of a hydrogen bubble on a vertical electrode is simulated in a cathodic half-cell compartment (30% KOH solution) (Fig. 6B) using equations of fluid flow, mass transfer, and tertiary current distribution.[158] The effect of flow rate and pressure on the growth of a single stagnant gas bubble is evaluated; an increase of both parameters ($\sim$1.2 to $\sim$40 mm s^{-1} and 1 to 40 bar for velocity and pressure, respectively) decreases the radius of the gas bubble by $\sim$20% and $\sim$82% (from $\sim$40 to $\sim$32 and $\sim$7 μm), respectively. CFD simulations are also employed to study the effect of electrolyte flow velocity and morphology of the nanostructured electrode on bubble dynamics (Fig. 6C).[150] The surface of the electrode contains hematite arrays with hydrophilic properties; these arrays have a large electrochemically active surface area and attract liquid into their structure *via* capillary action, creating a reactive liquid film favouring electrochemical reactions. As a result, the removal of formed gas bubbles is accelerated, and electrochemical reaction sites become mostly available due to minimal bubble adhesion, resulting in an increase in current density. A $\sim$4.3 mA cm^{-2} current density at 2 V (*vs.* RHE) is obtained for this modified electrode at $\sim$0.1 m s^{-1} flow compared to $\sim$3.5 mA cm^{-2} at no electrolyte flow.[150]

The second modelling approach of multiphase flow, namely the Eulerian approach, treats both dispersed (gas bubbles) and continuous phases (liquid electrolyte) as interpenetrating continua. It is based on averaging the Navier–Stokes equations (eqn (S1) and (S2) in ESI†) for each phase present.[160] Even though it does not allow the monitoring of individual bubble growth at the microscale, it requires a much lower computational cost than the E–L approach for simulating bubble dynamics at the macroscopic scale in water electrolysers.[161] It can provide an estimate of the bubble coverage of the electrode surface (an important parameter increasing cell overpotential) by measuring gas plume thickness.[162] A 2D two-fluid Euler–Euler model is developed for a water electrolysis cell of 12 cm length and 3 cm width.[163] Two 4 cm long vertical planar electrodes for the HER and OER are placed parallel to each other at a 3 mm gap and 40 mm distance from the bottom of the cell with an alkaline electrolyte in the channel. As the current is applied, gas bubbles evolve over the electrodes and form a diphasic boundary layer, which becomes thicker along

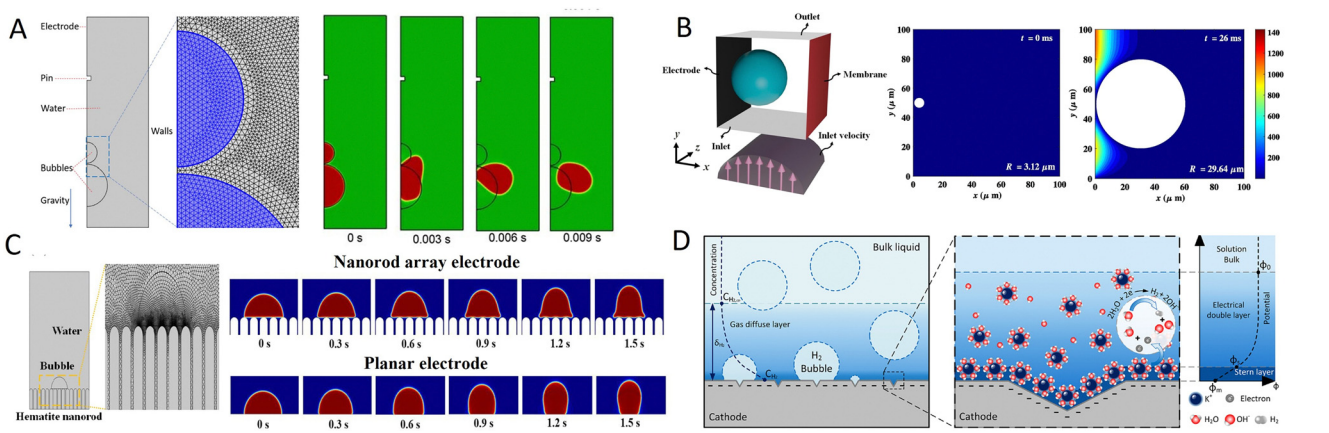

Fig. 6 Electrode models for gas bubble management. (A) Model of bubble coalescence on and detachment off a vertical gas-evolving electrode; reproduced with permission.[156] Copyright 2020, The Electrochemical Society and IOP Publishing. (B) Model of growth of single gas bubble of hydrogen at the cathode side of an alkaline electrolyser. Reproduced with permission.[158] Copyright 2019, Elsevier. (C) Effect of electrode morphology on bubble hydrodynamics. Reproduced with permission.[150] Copyright 2023, Elsevier. (D) Hydrogen bubble nucleation study on electrode surface in alkaline solution; reproduced with permission.[159] Copyright 2020, American Chemical Society.

the height of the electrodes. Increasing current density from 500 A m^{-2} to 2000 A m^{-2} results in an increase of the bubble void fraction (ε) and boundary layer thickness (δ) of both anode (ε_{an} from ~0.23 to ~0.33 and δ_{an} from ~515 μm to ~690 μm) and cathode (ε_{cath} from ~0.13 to ~0.19 and δ_{cath} from ~600 μm to ~800 μm). As electrolyte resistance increases with bubble void fraction, this model provides an important tool to optimise the operating conditions and cell design for effective bubble management.[163]

A 2D Euler–Euler model of multiphase flow has been developed for a porous HER electrode in alkaline electrolyte using the Euler–Euler model to investigate the impact of electrode surface properties on gas fraction.[164] In a stagnant electrolyte, an electrode with a superaerophobic surface facilitates bubble detachment and increases gas fraction; a decrease of electrode CA from 161.3° to 29.4° raises gas fraction from ~0.9% to ~1.4% at ~125 mA cm^{-2}. Furthermore, forced electrolyte flow can improve diffusive ion transport into the porous electrode by lowering the gas fraction near its surface; it is observed that an increase of flow velocity from ~1 to ~15 cm s^{-1} reduces the gas fraction from ~2.7% to ~1.3%.[164] Another Eulerian model of a parallel plate membrane-less electrolyser highlights the potential trade-offs between current density, efficiency, and product gas purity.[165] High-speed camera imaging is used to estimate the width of the generated downstream H_2 bubble plume in the cathode as an indicator of gas crossover. Exploration of various flowrates (from low Re ~ 131 to high Re ~ 1419) reveals that the smallest width of the bubble plume is achieved at Re ~ 796 for this electrolyser operating at 200 mA cm^{-2} in a 0.5 M H_2SO_4 electrolyte solution. A 1D model is used to estimate the required channel width for specific voltage efficiency (~45–85%) and current density (up to ~1000 mA cm^{-2}) for the safe operation (H_2 crossover <4%) of this device. The required channel width to achieve electrolyser efficiency >65% at ~400 mA cm^{-2} in an acidic solution (0.5 M H_2SO_4) should be less than 1.8 mm. For a more conductive alkaline electrolyte (30% KOH), the channel width can be increased to larger values (<2.6 mm) to achieve the same efficiency and current density. To reach >85% electrolyser efficiency while maintaining H_2 crossover below 4%, its channel width should be <0.5 mm and operated at a small current density (<25 mA cm^{-2}), demonstrating the structural and performance limitations of this design.[165]

4.1.2. Gas diffusion layer models. The porous gas diffusion layer (GDL), alternatively known as the porous transport layer (PTL), transports reactants and products to or out of the catalyst layer of an electrolyser, respectively.[166] Models reported in the literature examine the impact of the thickness or morphology of the GDL on water saturation in an electrolyser.[167,168] A thick GDL causes significant resistance in fluid flow and charge transport, however, reducing its value below ~0.25 mm results in water starvation of the device.[169] This experimental observation is confirmed by a 2D Multiphysics model of the PTL in a proton exchange membrane electrolyser cell (PEMEC) (Fig. 7A).[167] Electrolyser operation at a high current density of 5 A cm^{-2} with thin PTL (~100 μm) results in water starvation (1% liquid saturation) and very low current density (~0.5 A cm^{-2}). At lower current density (~2–3.5 A cm^{-2}), liquid saturation increases to ~10–20%. However, thicker PTLs (200 μm or 500 μm) show improved water saturation above 30% and uniform distribution of current density across the catalyst layer, signifying the importance of optimising PTL thickness to achieve good performance in water electrolysers.[167] The role of the pore size of a hierarchical GDL in the anode on electrolyser performance is also investigated.[168] A GDL containing large pores with ~406 mm diameter and ~203 mm spacing increases device performance by preventing oxygen gas buildup in the catalyst layer and drying of the membrane, compared to other GDLs containing pores of smaller diameter (~305 mm) and spacing (~152.5 mm). However, device performance becomes similar to the latter GDL when the GDL with the largest pores (~406 mm) has a lower number of available pores.[168]

Gas bubble dynamics in a PTL are highly dependent on the operating conditions of the electrolyser.[171] Modelling and high-speed camera visualisation of micropores of a PTL show that both current density and temperature increase bubble growth rate, whereas flowrate has no impact on bubble behaviour.

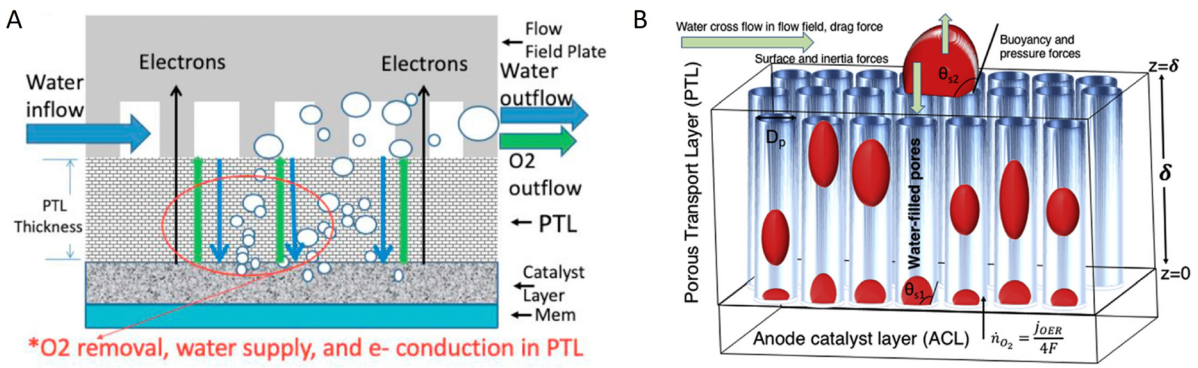

Fig. 7 Gas diffusion layer models: (A) 2D model of porous GDL of PEMEC to investigate the impact of its thickness on liquid saturation of the anode catalyst layer. Reproduced with permission.[167] Copyright 2020, Elsevier. (B) Model studying the effect of GDL wettability and pore size on oxygen bubble transport and overpotential. Reproduced with permission.[170] Copyright 2017, Elsevier.

Surface properties of a PTL can also significantly impact multiphase transport and gas bubble dynamics of water electrolysers. The impact of the wettability of the PTL and anode catalyst layer (ACL) on the growth and stability of three types of bubbles has been investigated (Fig. 7B): nucleation-driven, buoyancy-driven, and drag-driven.[170] While nucleation driven bubbles flowing inside the pores of PTL show an overpotential of ~28 mV, buoyancy- and drag-driven bubbles formed at the interface of the PTL and flow channel block the water transport to the PTL pores located underneath, resulting in larger overpotentials (~43 and 35 mV for buoyancy-driven and drag-driven bubbles, respectively). The wettability of the ACL and PTL affect significantly the bubble overpotential and their lifetime; the more hydrophilic they are (contact angle ~140°–175°), the smaller the bubble overpotential (~40 to 5 mV for drag-driven bubbles located on a hydrophilic ACL and ~55 to ~35 mV located on a hydrophilic PTL) and their lifetime (~3.4 to 2.6 s).[170]

4.1.3. Flow-field models. Apart from product gas removal from the GDL, the flow field distributes water through the GDL uniformly and prevents water flooding or starvation. Flow-field design plays a critical role in the performance of an electrolyser by affecting bubble dynamics, heat management, mass transfer, and electrode surface coverage.[172] Achieving uniform distribution of reactants and product gases in an electrolyser is often challenging. For example, three-dimensional modelling of two-phase flow in a parallel flow-field of a PEM electrolyser has been performed with the anode side subjected to a constant water flow of ~260 mL min^{-1} and varying oxygen generation rate of 0 to ~14 mg s^{-1}.[173] Simulations reveal that the oxygen volume fraction and velocity are not uniform across the flow-field with a higher oxygen fraction and lower velocity observed in its centre. This issue can be addressed by exploring various flow-field designs, such as serpentine and interdigitated (Fig. 8A).[174] The velocity distribution is relatively uniform in a serpentine flow-field, whereas in parallel and interdigitated flow-fields the velocity distribution is non-uniform: a peak velocity is observed at the inlet and outlet, whereas the velocity in the centre of these flow-fields is small, leading to slow transport of the reactants through the electrode. A similar trend is observed for the oxygen concentration across these flow-fields.[174] The effect of various circular designs of the flow-field on the hydrodynamic behaviour of a PEM electrolyser (Fig. 8B) is also examined *via* CFD simulations.[175] Three different inlet–outlet port configurations (designated as geometry 1, 2 and 3) of an anode PTL for a PEM electrolyser were considered to simulate the distribution profile of oxygen across each flow field. Even though the mean velocity of oxygen at the centre of each flow-field is similar within 0.1 m s^{-1}, the velocity fluctuates at the inlet and outlet ports (~5.7 m s^{-1} for geometry 1, ~2.95 m s^{-1} for geometry 2, and ~1.96 m s^{-1} for geometry 3). A difference in the mean oxygen volume fraction of each flow-field is observed as well; the flow-field with geometry 1 has the highest (~0.8), whereas the flow-field with geometry 3 demonstrates the lowest (~0.1) volume fraction, indicating that the latter flow-field can improve the performance of the PEM electrolyser, since the formed bubbles will be smaller than the ones in the flow-field with geometry 1.[175]

As design parameters of channels have a significant impact on multiphase flow and device performance, 3D simulations were performed to investigate the influence of various characteristics (height, wettability, upper wall geometry) of the microchannels of a PEMEC on bubble dynamics to optimise its design for favourable bubble detachment.[176] Visualisation by high-speed camera using transparent flow channels was employed to qualitatively show the four stages of bubble detachment based on the interplay of surface tension and forces of fluid flow: initial phase, instability, deformation, and detachment. The required power for the detachment of a ~100 μm bubble from a flow channel with 1 mm height and CA ~60° is ~60.8 μW; it was demonstrated that a reduction in CA (~30°) and height (~0.6 mm) of the flow-field can significantly decrease the parasitic losses, as the power required is significantly reduced to ~7 and ~33 μW, respectively. However, a

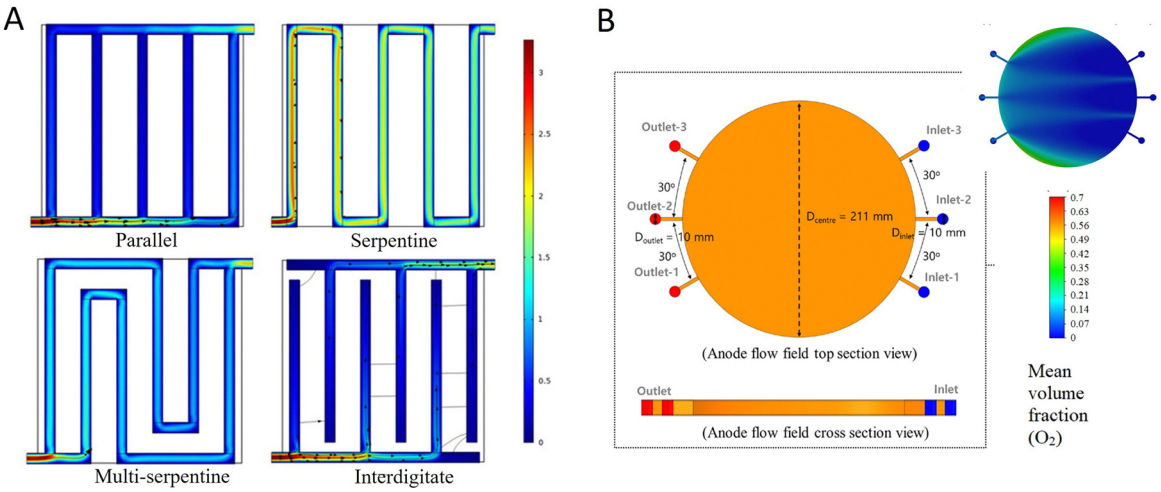

Fig. 8 Flow field models (A) effect of flow field designs (parallel, serpentine or interdigitate) on PEMEC cell performance. Reproduced with permission.[174] Copyright 2023, MDPI. (B) Effect of circular flow field design on the distribution of oxygen volume fraction in a PEMEC. Reproduced with permission.[175] Copyright 2023, Elsevier.

reduction in height of the flow channel will obstruct the flow of the electrolyte and, hence, the H_2 production efficiency of the electrolyser; to circumvent this issue, while maintaining the same low height of the flow channel, a waveform design (such as, sinusoidal and rectangular) can be employed for the engineering of the flow cell, minimising the power requirement for bubble detachment.[176] A 3D cell model has been developed using coupling of heat transfer, two-phase flow and electrochemistry to study the temperature evolution in alkaline electrolyser flow channels with zero-gap cell design configuration.[177] This showed is a non-uniform temperature distribution along the flow channels of the electrolyser and formation of local hot spots in the regions where gas bubbles are accumulated due to inadequate flow of the electrolyte. At higher current density ($\sim$4242 mA cm^{-2}) temperature uniformity deteriorates with maximum temperature variation along the *x*-axis reaching up to 5.1 K. A high flow rate ($\sim$2.1 *vs.* $\sim$0.9 ml min^{-1} cm^{-2}) can reduce the temperature difference in a cathode channel significantly (0.4 K *vs.* 3.6 K), whereas a higher inlet temperature (351.35 K *vs.* 303.15 K) can also aid in the reduction of the temperature variation (1.4 K *vs.* 2.2 K).

4.1.4. Pore network models (GDL and catalyst layer). Most of the reported models describing the transport processes of water electrolysers are continuum models. However, such an assumption is not applicable at the nanoscale, where conventional fluid dynamic equations cannot accurately describe fluid transport behaviour.[178] As the diameter of the pores in the GDL and catalyst layer (CL) is in the nanometres range, a mesoscopic pore network model (PNM) is needed to accurately describe the complex transport processes encountered through the porous media of these devices.[179] PNMs are popular in PEMFCs,[179] where they have been employed for the modelling of complex reactive processes in fuel cell catalyst layers,[180–182] as well as evaluating the water saturation of GDLs.[183,184] However, these mesoscopic PNMs are rarely utilised for multi-phase transport modelling in water electrolysers. Early models generate pore networks of iridium oxide (IrO_x) electrocatalyst in proton exchange membrane water electrolyser (PEMWE) *via* a stochastic method with two pore regions (below and above 250 nm),[185] and simulations are performed to correlate the CL's micro-structural properties with two-phase transport. The Bruggeman relation, widely employed in macroscopic models,[186–188] could be leveraged here for the estimation of water and gas permeation, as single- and two-phase permeability calculations show an order of magnitude difference for this CL having a porosity of 0.38 (a typical value for commercial CLs).[185] However, for calculating these two-phase properties, a higher value of the Bruggeman exponent ($\sim$4) has been recommended instead of the commonly used value of 1.5, due to variations in the pore diameter of this IrO_x CL having two distinct pore regions, where the assumption of homogenous tortuosity of the CL is invalid.[185]

To study the effect of pore diameter (d_{pore}) on two-phase transport properties, the pore network of a titanium-based PTL in a PEM electrolyser is numerically generated by stochastic modelling, possessing spherical pores connected through cylindrical throats.[143] The larger pores of the PTL show higher permeation for liquid water; at 36% oxygen coverage, a PTL with $d_{pore} \sim 33.5$ μm has a two-phase water permeability of $\sim 5.5 \times 10^{-13}$ m^2, which is higher than the $\sim 1 \times 10^{-13}$ m^2 for a PTL with $d_{pore} \sim 26.5$ μm. The effect of the porosity gradient between the PTL-catalyst coated membrane (CCM) interface and PTL-flow-field interface is examined by employing two PTLs with specific structural properties obtained from micro-tomography (25–65% gentle gradient, GG-PTL and 8–85% steep gradient, SG-PTL). SG-PTL shows lower $\sim$15% gas saturation than GG-PTL at its centre, causing higher water permeation (3×10^{-13} m^2), and suggesting that a lower porosity at the PTL-CCM interface can further improve reactant transport through PTLs.[143] The design parameters of these PTLs can be optimised by investigating the impact of particle diameter (d_P) of precursor titanium powder and PTL porosity (ε) on reactant transport.[144] As d_P increases from $\sim$25 μm to $\sim$75 μm, the two-phase water permeability increases significantly from $\sim 6.37 \times 10^{-14}$ m^2 to $\sim 76.9 \times 10^{-14}$ m^2. Although higher porosity yields improved water permeation, it also increases the surface roughness and contact resistance of the PTL. This effect is more prominent at porosity values above 40% leading to severe PTL roughness of $\sim$80 μm and, thus, to performance losses. To overcome this issue, a PTL with $d_P \sim 25$ μm and $\varepsilon \sim 0.265$ is suggested for electrolyser operation at intermediate current density, while a PTL with $d_P \sim 25$ μm and $\varepsilon \sim 0.405$ is suggested for electrolyser operation at high current density.[144]

4.1.5. Other electrolyser layers models. There are limited modelling reports of other electrolyser layers, such as electrocatalyst, membrane, *etc.* A gradient-distributed catalyst layer (CL) design in a PEMWE using a 2D numerical model has been developed, showing a 7% increase in current density at 2.4 V compared to a uniform CL.[189] Such CL design with linear variation of agglomerate radius size (average size $\sim$1 μm) from membrane to GDL interface could reduce precious metal loading, with total catalyst and ionomer loading of 1.0 mg cm^{-2}. However, it results in a slight temperature rise (1–2 °C) within the PEM, which may affect long-term stability. Another 2D numerical model investigates different electrocatalysts for improved OER efficiency.[190] Utilisation of Pt–Ir instead of Pt results in a fourfold increase in current density, while the hydrogen molar fraction in the cathode gas channel increases by 60%.[191]

A current–voltage and gas crossover model has been developed for a zero-gap alkaline electrolyser with $\sim$20 N m^3 h^{-1} hydrogen generation capacity. The impact of the thickness of the diaphragm (100–500 μm), temperature (60–100 °C) and pressure (1–50 bar) on electrolyser performance with minimum gas crossover has been investigated. Simulation results show that a current density up to 1.6 A cm^{-2} is achievable for a zero-gap cell design *vs.* 0.4–0.6 A cm^{-2} for a conventional alkaline cell design by reducing the thickness of the diaphragm up to 0.1 mm and using the higher temperature of 100 °C. However, such alterations cause high gas crossover, which must be decreased below 10% *via* operation below 8 bar.[191] A 1D numerical model of an MEA has been developed for investigating the effect of temperature on the membrane degradation in a PEMWE (25 cm^2).[192] The production of fluoride ions is increased

as temperature climbs from 333 K to 353 K, while the thickness of the membrane is reduced by half after ~380–500 h of operation at 333 K and ~80–700 h at 353 K, emphasising the need for optimised operating conditions to extend electrolyser lifespan.[192]

4.2. Complete cell models

There are several reports in the literature of complete cell models to study the effect of the operating conditions and design parameters on electrolyser performance.[193,194] Apart from standard equations of charge transfer and kinetics, which are used to model electrode layers in such models, the overall cell voltage (V_{cell}) is composed of several components: open-circuit voltage (V_{ocv}), the activation overvoltage (V_{act}), the ohmic overvoltage (V_{ohm}) and the mass transport or diffusion overvoltage (V_{diff}), which are described by eqn (S3)–(S11) in the ESI.† Complete cell models are usually three-dimensional (3D) to investigate coupled physicochemical phenomena encompassing electrochemical reactions, mass transport, and capillary flow of multiple phases within cathodic/anodic channels and porous gas diffusion layers (Fig. 9A and B).[195,196] For a PEM electrolyser, an increase in the porosity of the GDL from ~0.2 to ~0.6 results in lower water saturation in the cathode diffusion layer (CDL), *i.e.* ~0.21 and ~0.19 for the previously mentioned porosity values of the GDL.[195] The opposite effect is observed at the anode diffusion layer (ADL), as the water saturation increases with porosity (~0.55 and ~0.61 at ~0.2 and ~0.6 porosity, respectively). This is due to the enhancement of capillary flow as the porosity of the GDL increases, transporting water rapidly from the cathode to the anode.[195] A similar result is obtained with the alteration of the hydrophobicity of the GDL, since any increase decreases the capillary pressure and, hence, capillary flow, leading to water transport from CDL to ADL.[196] However, to avoid water starvation or flooding of the catalyst layer, the hydrophobicity of the GDL should be higher than the ACL's. Under such conditions, the direction of capillary pressure from the ACL to GDL promotes the detachment of the generated gas bubbles from the ACL, resulting in an increase in H_2 production efficiency (~13%).[196]

The impact of thermal limitations on electrolyser performance at high current density is investigated *via* a 1D thermal model and validated with experimental measurements in a 5 cm^2 cell.[177] At high current densities up to 25 A cm^{-2}, significant heat (up to 35.5 W cm^{-2} compared to ~1 W cm^{-2} for today's PEMWE typical current density range of 1–2 A cm^{-2}) is generated due to ohmic and activation losses, leading to increased MEA temperatures (~90 °C). This excessive heating without proper cooling management accelerates membrane and catalyst degradation. To avoid this, high water flow rates (~25 ml min^{-1} cm^{-2} at 10 A cm^{-2}) are essential for effective dissipation of the heat produced (~5.7 W cm^{-2}) and stable operation. The possibility to use such higher current densities can result in a significant reduction in material usage and

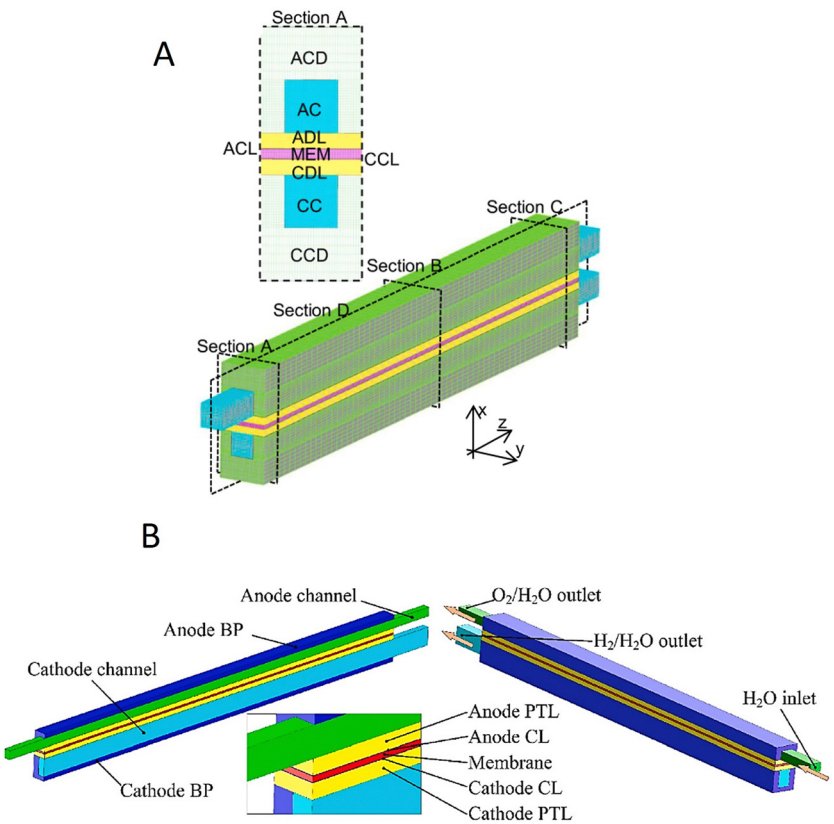

Fig. 9 Geometries for various cell models of water electrolysers: (A) 3D model of PEM design. Reproduced with permission.[195] Copyright 2022, Elsevier. (B) 3D model of PEM design with single channel and multiphase flow. Reproduced with permission.[196] Copyright 2022, Elsevier.

device cost, ultimately paving the way to meet the future goal of their large-scale application.[177]

The integration of electrolyser technologies with renewable power is often required in practical conditions. This is investigated in Multiphysics modelling to optimise the design of industrial alkaline water electrolysis (AWE) stacks under varying load conditions when coupled with renewable energy sources.[197] Small cell (SC) design has a higher number of smaller cells, resulting in a reduction of bubble coverage (~12.5% lower volume fraction near the electrode) and an increase of hydrogen production (~6.7% higher at 2.3 V) under heavy loads (on-grid scenario). However, under light and dynamic load conditions, SC suffers from high shunt currents, leading to lower efficiency. For off-grid scenarios, such as the use of wind power, large cell (LC) design, which has fewer but larger cells, is more suitable as it minimises shunt currents and improves current efficiency (~20% higher at 1.7 V). However, the longer flow channels in LC design result in a larger bubble curtain, which can negatively impact the contact between electrolyte and catalyst.[197] Integration with renewable power sources is further explored in system-level models, encompassing the entire electrolysis stack, balance of plant (BOP) and power supply.[198,199]

Thus far, there are limited reports on numerical models for membrane-less electrolysers.[60,165,200] An analytical multiphase flow model has been developed for a parallel-plate electrolyser without a separator, focusing on gas–liquid flow dynamics.[200] By quantifying the gas fraction profile of bubble plumes along the vertical electrodes, it estimated the maximum height of the membrane-less electrolyser required for safe operation at specific interelectrode distance and flow velocity. At 1000 mA cm^{-2}, a buoyancy-driven membrane-less electrolyser with a 3 mm inter-electrode distance can achieve a maximum height of ~7.6 cm while maintaining 98% product purity at atmospheric pressure. However, by introducing forced flow at Re = 1000, the same electrolyser can be scaled up to ~17.6 cm.[200] Increasing the operating pressure can allow a further increase in its height, as the bubble size is reduced, enhancing gas dissolution.[200] The effect of cell geometry on the efficiency of membrane-less electrolysers is also investigated *via* numerical simulations and experimental validation.[60] A Y-shaped cell geometry is introduced as an optimised design compared to a flow-through T-shape or straight I-shape cell design. The Y-shaped cell design provides more uniform current distribution and increased efficiency, whereas T- and I-shaped cell designs suffer from non-uniform bubble accumulation, leading to increased local resistance and higher voltage losses. The cell voltage can be reduced further by ~0.17 V for Y-shaped electrolyser at a current density of 250 mA cm^{-2} by increasing the flow rate (Re ~ 1500).[60]

Overall, electrolyser numerical models offer critical insights from fundamental microscale phenomena to system-level optimisation. Although current models can describe electrode kinetics, bubble dynamics, mass transport and fluid flow, challenges lie in Multiphysics complexity and scalability. Addressing this gap will require the refinement of current electrolyser models and the development of multiscale models through integrated computational approaches.

5. Development of water electrolyser technologies from an industrial perspective

5.1. Technoeconomic context

PEM and alkaline electrolysers (AWE) remain the most mature technologies with several large-scale manufacturers in the USA (Plug Power and Proton onsite), Europe (ITM Power, NEL Hydrogen, ThyssenKrupp) and China (LongGi, PERIC Hydrogen and Tianjin Mainland).[201] Among alkaline electrolysers, atmospheric technology remains much more mature than pressurised technologies where there remain many questions about the operational limits. Besides, several challenges need to be addressed by 2050 in the development of very large-scale electrolyser plants. This includes enhancement of current densities (>2 A cm^{-2} for alkaline from current ~0.2–0.8 A cm^{-2} and up to 4–6 A cm^{-2} for PEM from current ~1–2 A cm^{-2}) to increase the hydrogen production rates and improve the energy efficiency (<45 kW h per kg_{H_2} from current ~50–70 kW h per kg_{H_2}) to reduce power consumption.[18] Other 2050 targets include operation possibly at higher pressure (>70 bar *vs.* current <30 bar) and increasing the stack unit size to 10 MW from 1 MW along with doubling its lifetime to ~100 000 h and above.[18] An important challenge for such a massive scale-up is to bring down the current high cost of electrolytic hydrogen to a much lower level (<2 $ per kg) to make it competitive enough with other hydrogen production technologies on the market, notably steam methane reforming, which had a 45% market share in 2020.[202] This will require reduction of both capital expenditure (CAPEX) and operational expenditure (OPEX).

The high production cost (OPEX) of electrolytic hydrogen is mainly because of the high cost of electricity. The electricity costs represent the largest share of the renewable H_2 production technical cost from 50% up to 80% depending on the geographical zone. Moreover, grid electricity cannot meet the total demand of electricity consumption while scaling up the electrolysers to GW scale. For example, if all of today's hydrogen demand is to be met by water electrolysers with 60% assumed efficiency, it will require 3600 TW h of electricity consumption, which exceeds the total grid electricity generated in Europe annually.[20] Electricity from renewable sources, such as solar or wind, can bring down its cost to make it more affordable.[203] That is why large GW-scale plant projects are envisaged in regions with the highest load factors of wind or sun to benefit from the lowest possible levelised cost of electricity (LCOE). In this context, it is essential to maximise the conversion rate from the produced electrons to hydrogen. As an illustration, if one considers an islanded plant delivering 75 kt per year of green H_2 (powered roughly by 1 GW of renewables): the increase of the energy efficiency of the electrolysis plant by 10% may reduce the global electricity expenditure by more than 400 M$ with a 55 $ per MW h electricity price over the project life. In addition to the reduction of the electricity OPEX, substantial efforts are required to decrease at the same time the installation cost of electrolysers (CAPEX). This should be achieved by automating the manufacturing processes and the use of affordable materials. For a minimum 10 MW electrolyser plant, total installed system CAPEX for alkaline (~500–1000 $ per kW) and PEM (~700–1400 $ per kW) electrolysers reported in

2020 – numbers that are even higher if one consider the full installation costs – are far away from the 2030 CAPEX target (<200 $ per kW).[18] Stack cost, which is a major component of CAPEX, is expected to decrease significantly by 2030 to 52–79 € per kW for alkaline and 63–234 € per kW for PEM electrolysers respectively, while ramping up their stack power densities from 0.5 W cm^{-2} to 2.3 W cm^{-2} and 4.75 W cm^{-2} to 6.3 W cm^{-2}, respectively.[204]

5.2. Technological status and development

5.2.1. PEM and AWE. A cost breakdown for 1 MW PEM and AWE electrolysers is given in Fig. 10 for comparison from cell level (membrane/diaphragm electrode assembly) to stack and full system based on IRENA estimates in 2020.[18] For a PEM, electrode catalysts and bipolar plates constitute 10% and 50% of electrolyser stack cost, respectively.[20]

Electrocatalyst development with advanced architectures and manufacturing techniques will play a critical role in GW-scale electrolyser deployment.[205] Current catalysts are not only expensive materials (Pt, Ir) but have limited supplies. For example, finding an alternative to Ir and/or being able to recycle it fully is crucial, because of its very limited availability worldwide. As of today, the iridium requirement in a PEM stack

Fig. 10 Cost breakdown for PEM and AWE technologies from a single cell (membrane electrode assembly) to a complete stack (1 MW electrolysers), reproduced from the International Renewable Energy Agency Report: Green Hydrogen Cost Reduction.[18] Copyright 2020, IRENA.

is around 0.75 kg per MW, while the annual global iridium production ranges from 8 to 9 tonnes. One can reasonably consider that around 20% of today's iridium supply could be allocated to electrolyser production, which would allow the construction of only 2 or 3 GW of PEM electrolysers.[206] Those figures must be put in comparison to electrolyser production forecasts. IRENA estimates an average of 160 GW annually installed electrolyser capacity over the next 25 years to meet the demand objective of renewable H_2.[207] By combining such a capacity with IEA's predictions of a 90% alkaline to 10% PEM ratio, the future stress on iridium is not negotiable. Technological breakthroughs are required in current electrode catalysts to significantly reduce the amount utilised of these rare and expensive noble metals; it is expected to decrease iridium loading on the anode to 0.2 mg cm^{-2} and platinum loading on the cathode to 0.05 mg cm^{-2} by 2030.[18] Nanostructured electrocatalyst design strategies, *e.g.* alloying, doping, size reduction to small nanoparticles or single atoms and loading on advanced nanocarbon supports can assist in achieving these targets.[208]

The stability of a PEM electrolyser is highly dependent on the durability of MEA components and operating conditions, including temperature, current density, and water flow rate. To translate any lab scale PEM electrolyser to a commercial product, accelerated stress tests (ASTs) of MEA components are essential. These tests are extensively discussed in recent reviews[209–211] for evaluating the feasibility of PEM electrolysers for industrial deployment in long-term operation. With a long PEM electrolyser operational lifetime of ~50 000 h, high electrocatalyst stability is needed to maintain the stack performance. Many phenomena, such as morphology change, metal dissolution and surface passivation, can lead to voltage deterioration during the industrial operation of an electrolyser.[212] This opens the question of the duration of stability tests of catalysts in the literature: roughly limited to 100 h, such results are insufficient to be able to anticipate the catalyst's behaviour in an industrial context and potentially transfer the technology. Electrocatalyst durability testing is often neglected in laboratory studies where performance degradation testing of an MEA for an initial few thousand hours (~4000 h) can even provide some insights into catalyst stability.[213] As the Ir catalyst in the anode is more prone to degradation at high potentials (>1.8 V), its stability can be better evaluated in shorter time by various ASTs such as potential cycling between 1.45 to 2 V at 80 °C and a square-wave current cycling between 0.1–1 A cm^{-2} for 100 h.[209] From a CAPEX point of view, bipolar plates represent a major portion (~50%) of the stack cost. They are based on titanium coated with noble metal: platinum-coated titanium at the anode and gold-coated titanium at the cathode. Research on alternative materials like carbon-based bipolar plates is an interesting route for cost optimisation of the stack.[214] Chemical, thermal or mechanical degradation of the membrane can occur under various stressors; membrane degradation occurs due to radical attack at the weak links (end groups) of the perfluorosulfonic membrane, which is accelerated at high current densities (>2 A cm^{-2}). As the membrane backbone is attacked by oxidative species, fluorine and sulphur are released.[209,210] The porous transport layer (PTL) at the anode side is more prone to chemical degradation due to higher voltage and oxygen-rich environment compared to the cathode side. The anode PTL, which is typically titanium-based, experiences passivation, hydrogen embrittlement, and conductivity loss over time.[209] An AST for PTL stability involves constant current operation (2 A cm^{-2} for 1000 h) demonstrating that Ti passivation increases ohmic resistance, which can be reduced by 89% with Pt-coating.[210] Carbon corrosion can occur at the gas diffusion layer (GDL) at the cathode side. An AST for GDL involves its immersion in 35% H_2O_2 at 90 °C for 12 h, resulting in loss of its hydrophobicity and increased water flooding. Furthermore, an AST for evaluating GDL mechanical stability involves cyclic compression (1.4–3.4 MPa, ~5 cycles), resulting in structural changes in the GDL, such as cracks and reduced porosity.[210]

Alkaline electrolyser stacks are indeed 2 to 3 times less expensive than PEM stacks as they use non-noble catalysts, typically nickel, coupled with nickel bipolar plates, making the technology more attractive in terms of CAPEX compared with PEM electrolysis. The reduction in costs of materials in alkaline electrolysers is not trivial, especially since the price of nickel could rise if a context of strong demand emerges. However, the tendency regarding the development of new catalysts is less driven by cost reduction than by an increase in catalytic activity to promote the cells' current density. This improved performance must persist over the long term with low degradation rates, as, in practice, the operating voltage of current electrolyser stacks degrades by ~0.4–5 μV h^{-1}, leading to a 10% lower performance after ~40 000 h of operation compared to the startup.[20] Therefore, it is important to develop longer-lasting tests and relevant accelerated stress tests that could better extrapolate to real operational conditions of alkaline electrolysers.[215] Moreover, electrocatalyst testing at industrially relevant harsher conditions such as a high temperature (70 °C *vs.* 25 °C in the laboratory) and using more concentrated electrolytes (6.9 M *vs.* 1 or 0.1 M KOH in the laboratory) is required.[216] For alkaline electrolysers, an intermittent rather than continuous operation puts stress on electrodes, causing irreversible changes by catalyst dissolution and performance degradation. Therefore, the development of catalysts is needed that are more robust to reverse currents to handle dynamic load changes of renewable energy sources.[216] Scaling up electrocatalyst synthesis from laboratory milligram scale to industrial kilogram scale requires the development of high-throughput production methods such as a roll-to-roll method demonstrated for manufacturing catalyst thin films of 5 m length and 0.25 m width for alkaline water electrolysis.[217] The development of alternative diaphragms that are stable at high temperatures while maintaining conductivity could be relevant, as a reduction in overpotential by increasing temperature can be achieved (~2.3 to 3.6 mV $°C^{-1}$ for the temperature range of 50–200 °C, while operating at a current density of 1 A cm^{-2}).[216] However, the current state-of-the-art Zirfon diaphragm limits the electrolysis operation below 100 °C. Utilising zero-gap designs and thinning diaphragms down to 150 μm should lead to a major increase in efficiency of these devices in the future.

Moreover, corrosion of stainless-steel equipment of the balance of stack (BoS) can take place during pressurised alkaline electrolyser operation, releasing some impurities that can impact the electrode quality. Exogenous and endogenous impurities from various sources can impact the electrolytic performance of the cell by catalyst poisoning, lowering membrane conductivity, *etc.*[218] but it is seldomly studied in literature. For example, iron oxide impurities are released in alkaline electrolysers due to the corrosion of stainless-steel equipment exposed to KOH in 30 wt% lye. Some of those iron particles are trapped by the mechanic and/or magnetic filters that can be present in the lye circulation loop of the BoS, but soluble impurities and fine particles can go through it, causing some deposition on and/or insertion in the electrodes. Demnitz *et al.* showed recently the growth of iron dendrites on the Ni cathodes of alkaline electrolyser in presence of iron dissolved in the lye.[219] That being said, we must question the stability of new catalysts (which generally contain a fraction of noble metals) under aged electrolyte conditions, since they could be more sensitive to metallic impurities or traces, which would impact their expected performance over time.

5.2.2. Potential development axes. In this context, the development of a new generation of electrolysers operating under 15–30 barg pressure, going toward corrosion-free design, would constitute a key advance to maximise the stability of the electrodes by preventing them from impurities. This means either using a stable coating in existing metallic equipment or replacing them by polymeric elements.

Typically, membrane-less or capillary-fed electrolyser cell/stack designs discussed in Section 2.2 are attractive, since, *via* potentially relevant choices of materials and simplification of designs, they could fulfil the requirements mentioned above in terms of material stability to corrosion or operating temperature range. This would allow a reduction in CAPEX and potentially OPEX in case of increased energy efficiency of the system. Nevertheless, at that stage, the real impact of such cell designs on gas separation *via* the control of flux of the electrolyte or gas in the vicinity of the electrodes remains to be demonstrated at a larger scale (MW system).[53] All those new approaches in cell (Section 2.2) and electrode design (Section 3) are still at an early stage and far from large deployment, but this opens the route to potential breakthroughs in the long term.

From a shorter-term perspective, the anion exchange membrane (AEM) or solvating membrane (like PBI) appears as a promising route for optimising alkaline-based systems. AEM can be much thinner than traditional diaphragms with better gas tightness, significantly reducing ohmic losses and optimising the energy efficiency of the cells when paired with non-noble catalysts.[220] For AEM water electrolysis, membrane degradation is a major concern due to its chemical instability in an alkaline environment, while the noble metal-free electrocatalysts are susceptible to corrosion over extended operation ($\geq$300 h).[221] Despite advances in AEM membrane chemistries enhancing stability, additional fundamental research is needed to optimise this technology. Specifically, developing tailored ionomers and catalysts for low-concentration electrolytes or pure water and a better understanding of the catalyst/ionomer/membrane interactions are crucial to compete with traditional technologies in performance and lifespan for industrial-scale deployment.[222]

5.3. Operation perspective

From an operational point of view, beyond safety aspects, the efficiency and reliability of the production plants are compulsory. Accordingly, the question of the real stack efficiency and performance decay over time is of paramount importance, since the repeated unexpected change of stacks would have a drastic impact on the maintenance costs. Typically, the operational lifespan of an electrolyser stack is expected to be between 8 to 10 years. This limitation of replacement OPEX costs is necessary to ensure the economic viability of any projects for large production of green H_2.

That is why R&D on new designs of materials, cells (Section 2) and stacks are still necessary to optimise performance and/or reduce costs. For example, new electrode designs mentioned in Section 3, based on hydrophilic or hydrophobic material solutions[28,108] for gas removal are attractive, since the management of bubbles and dissolved gas is of paramount importance to reduce the gas crossover. A reduction of the latter is particularly interesting to optimise the operational range of the electrolyser system.

The modelling of the different elements of the cells/stacks will help to promote future optimised architectures of cells and stack designs. Modelling is also very useful at a system level to optimise industrial operations. At that stage, acquiring operational data on real stacks remains the Holy Grail to feed and refine models. Building stack models integrating the ageing aspect would be extremely beneficial for supporting operations by developing predictive maintenance tools.

6. Conclusions

Green hydrogen production by water electrolysis can help to fight climate change, which has arisen mainly due to the enormous increase in energy produced from fossil fuels in the past century, raising it from $\sim$23 to $\sim$548 EJ.[223] However, to meet the United Nations' goal of net zero carbon emissions by 2050, widespread GW-scale hydrogen production is required, which is a significant increase from the current installed capacity at the MW-scale, dominated by PEM and alkaline electrolyser technologies. Several challenges need to be addressed to achieve this target of developing very-large-scale electrolyser plants, such as reduction of cost of electrolytic hydrogen ($<$2 \$ per kg), enhancement of current densities ($>$2 A cm^{-2} for alkaline and 4–6 A cm^{-2} for PEM) and improvement of the energy efficiency ($<$45 kW h per kg_{H_2}). Bubbles (10–800 μm) generated in water electrolysis cover the electrode, blocking its surface and degrading the cell performance substantially (overpotential of $\sim$308 mV at current density above 500 mA cm^{-2}). Therefore, the latest electrode designs reported in the literature have been comprehensively reviewed for effective bubble management of the water electrolysis reactions (HER and OER),

based on either bubble mitigation strategy (aerophobic electrode) or transportation strategy (aerophilic electrode). As models can aid experiments and accelerate technological development, the latest advancements in the modelling of water electrolysers have been reviewed, from complete cell models to more specific layer models. Membranes used in water electrolysers for separation of product gases pose challenges of high electrical resistance ($\geq$0.2 Ω cm^2) and thermal degradation above 90 °C. As a result, a new generation of membrane-less electrolysers has emerged within the last decade whose cell designs and electrochemical performance have been reviewed here. Despite various promising new designs of membrane-less electrolysers, several challenges remain to be addressed for achieving their commercial viability. Future research should focus on developing scalable and robust designs, improving gas separation and safety, and ensuring their long-term stability. Efficiency at the stack and system level needs to be evaluated for any proposed new cell design, along with techno-economic analysis and integration with renewable energy sources, to compete with existing electrolysis technologies.

Nomenclature

1D	One-dimensional
2D	Two-dimensional
3D	Three-dimensional
ACL	Anode catalyst layer
ADL	Anode diffusion layer
AE	Auxiliary electrode
AEM	Anion exchange membrane
AI	Aerophilic
AO	Aerophobic
AWE	Alkaline water electrolysis
CA	Contact angle
CAPEX	Capital expenditure
CCM	Catalyst coated membrane
CDL	Cathode diffusion layer
CL	Catalyst layer
EU	European Union
FC	Fuel cell
GDL	Gas diffusion layer
HC	Honeycomb
HER	Hydrogen evolution reaction
LDH	Layered double hydroxide
MEA	Membrane electrode assembly
NC	Nanocone
NF	Nickel foam
OER	Oxygen evolution reaction
OPEX	Operational expenditure
PEM	Proton exchange membrane
PEMEC	Proton exchange membrane electrolysis cell
PEMWE	Proton exchange membrane water electrolyser
PFAS	Polyfluoroalkyl substances
PNMs	Pore network models
PEI	Polyethylenimine
PE	Polyethylene
PS	Polystyrene
PSD	Pore size distribution
PTFE	Polytetrafluoroethylene
PTL	Porous transport layer
RDE	Rotating disk electrode
RHE	Reversible hydrogen electrode
RPM	Revolutions per minute
SAB	Superaerophobic
SAL	Superaerophilic
SHE	Standard hydrogen electrode
WE	Water electrolyser

Data availability

No primary research results, software or code have been included and no new data were generated or analysed as part of this review.

Conflicts of interest

There are no conflicts to declare.

Acknowledgements

The authors gratefully acknowledge funding from TotalEnergies and EPSRC through an EPSRC ''Frontier Engineering: Progression'' Grant (EP/S03305X/1), supporting nature-inspired electrochemical research in the UCL Centre for Nature-Inspired Engineering (CNIE).

References

1 IEA (2024), Electricity 2024: Analysis and forecast to 2026, International Energy Agency, Paris. https://www.iea.org/reports/electricity-2024.
2 R. J. Andres, D. J. Fielding, G. Marland, T. A. Boden, N. Kumar and A. T. Kearney, *Tellus B*, 1999, **51**, 759–765.
3 J. Delbeke, A. Runge-Metzger, Y. Slingenberg and J. Werksman, *Towards a climate-neutral Europe*, Routledge, 2019, pp. 24–45.
4 S. Baruch-Mordo, J. M. Kiesecker, C. M. Kennedy, J. R. Oakleaf and J. J. Opperman, *Environ. Res. Lett.*, 2019, **14**, 1–8.
5 W. Lubitz and W. Tumas, *Chem. Rev.*, 2007, **107**, 3900–3903.
6 N. Dubouis, D. Aymé-Perrot, D. Degoulange, A. Grimaud and H. Girault, *Joule*, 2024, **8**, 883–898.
7 P. Nikolaidis and A. Poullikkas, *Renewable Sustainable Energy Rev.*, 2017, **67**, 597–611.
8 B. Vivanco-Martín and A. Iranzo, *Energies*, 2023, **16**, 3866.
9 E. Gregor and J. Liselotte, *EU hydrogen policy: Hydrogen as an energy carrier for a climate-neutral economy*, European Parliamentary Research Service, 2021.

10 K. Scott, in *Electrochemical Methods for Hydrogen Production*, ed. K. Scott, The Royal Society of Chemistry, 2019, ch. 1, pp. 1–25.
11 E. Amores, M. Sánchez, N. Rojas and M. Sánchez-Molina, *Sustainable Fuel Technologies Handbook*, 2021, ch. 9, pp. 271–313.
12 H. Zhao and Z. Y. Yuan, *Adv. Energy Mater.*, 2023, **13**, 2300254.
13 H. Shin, D. Jang, S. Lee, H.-S. Cho, K.-H. Kim and S. Kang, *Energy Convers. Manage.*, 2023, **286**, 117083.
14 IRENA, *Decarbonising hard-to-abate sectors with renewables: Perspectives for the G7*, International Renewable Energy Agency, Abu Dhabi, 2024.
15 F. Frieden and J. Leker, *Sustainable Energy Fuels*, 2024, **8**, 1806–1822.
16 The European hydrogen market landscape: A report by European Hydrogen Observatory, 2023. **https://observatory.clean-hydrogen.europa.eu/tools-reports/observatory-reports**, 2023.
17 M. Chatenet, B. G. Pollet, D. R. Dekel, F. Dionigi, J. Deseure, P. Millet, R. D. Braatz, M. Z. Bazant, M. Eikerling, I. Staffell, P. Balcombe, Y. Shao-Horn and H. Schafer, *Chem. Soc. Rev.*, 2022, **51**, 4583–4762.
18 E. Taibi, H. Blanco, R. Miranda and M. Carmo, IRENA (2020), *Green Hydrogen Cost Reduction: Scaling up Electrolysers to Meet the 1.5 °C Climate Goal, International Renewable Energy Agency, Abu Dhabi*.
19 *RePowerEU Plan: Joint European action on renewable energy and energy efficiency*, **https://www.iea.org/policies/15691-repowereu-plan-joint-european-action-on-renewable-energy-and-energy-efficiency**.
20 M. Yue, H. Lambert, E. Pahon, R. Roche, S. Jemei and D. Hissel, *Renewable Sustainable Energy Rev.*, 2021, **146**, 111180.
21 A. J. Shih, M. C. O. Monteiro, F. Dattila, D. Pavesi, M. Philips, A. H. M. da Silva, R. E. Vos, K. Ojha, S. Park, O. van der Heijden, G. Marcandalli, A. Goyal, M. Villalba, X. Chen, G. T. K. K. Gunasooriya, I. McCrum, R. Mom, N. López and M. T. M. Koper, *Nat. Rev. Methods Primers*, 2022, **2**, 84.
22 K. Ayers, N. Danilovic, R. Ouimet, M. Carmo, B. Pivovar and M. Bornstein, *Annu. Rev. Chem. Biomol. Eng.*, 2019, **10**, 219–239.
23 K. O. Obodo, C. N. M. Ouma and D. Bessarabov, *Power to Fuel*, Academic Press, 2021, ch. 2, pp. 17–50.
24 J. W. Haverkort and H. Rajaei, *J. Power Sources*, 2021, **497**, 229864.
25 R. Wu, Z. Hu, H. Zhang, J. Wang, C. Qin and Y. Zhou, *Langmuir*, 2024, **40**, 721–733.
26 C. V. M. Inocêncio, Y. Holade, C. Morais, K. B. Kokoh and T. W. Napporn, *Electrochem. Sci. Adv*, 2022, **3**, 1–52.
27 M. Bernt, A. Hartig-Weiß, M. F. Tovini, H. A. El-Sayed, C. Schramm, J. Schröter, C. Gebauer and H. A. Gasteiger, *Chem. Ing. Tech.*, 2019, **92**, 31–39.
28 G. F. Swiegers, R. N. L. Terrett, G. Tsekouras, T. Tsuzuki, R. J. Pace and R. Stranger, *Sustainable Energy Fuels*, 2021, **5**, 1280–1310.
29 D. Zhang and K. Zeng, *Ind. Eng. Chem. Res.*, 2012, **51**, 13825–13832.
30 S. Yuan, C. Zhao, X. Cai, L. An, S. Shen, X. Yan and J. Zhang, *Prog. Energy Combust. Sci.*, 2023, **96**, 101075.
31 B. Bensmann, A. Rex and R. Hanke-Rauschenbach, *Curr. Opin. Chem. Eng.*, 2022, **36**, 100829.
32 S. A. Grigoriev, P. Millet, S. V. Korobtsev, V. I. Porembskiy, M. Pepic, C. Etievant, C. Puyenchet and V. N. Fateev, *Int. J. Hydrogen Energy*, 2009, **34**, 5986–5991.
33 P. Trinke, P. Haug, J. Brauns, B. Bensmann, R. Hanke-Rauschenbach and T. Turek, *J. Electrochem. Soc.*, 2018, **165**, F502–F513.
34 A. S. Emam, M. O. Hamdan, B. A. Abu-Nabah and E. Elnajjar, *Int. J. Hydrogen Energy*, 2024, **64**, 599–625.
35 N. Guillet and P. Millet, *Hydrogen Production*, 2015, ch. 4, pp. 117–166.
36 S. S. Kumar and H. Lim, *Sustainable Energy Fuels*, 2023, **7**, 3560–3583.
37 M. S. Thomassen, A. H. Reksten, A. O. Barnett, T. Khoza and K. Ayers, *Electrochemical Power Sources: Fundamentals, Systems, and Applications*, 2022, pp. 199–228.
38 N. Du, C. Roy, R. Peach, M. Turnbull, S. Thiele and C. Bock, *Chem. Rev.*, 2022, **122**, 11830–11895.
39 H. A. Miller, *Curr. Opin. Electrochem*, 2022, **36**, 101122.
40 S. E. Wolf, F. E. Winterhalder, V. Vibhu, L. G. J. de Haart, O. Guillon, R.-A. Eichel and N. H. Menzler, *J. Mater. Chem. A*, 2023, **11**, 17977–18028.
41 A. Hauch, R. Kungas, P. Blennow, A. B. Hansen, J. B. Hansen, B. V. Mathiesen and M. B. Mogensen, *Science*, 2020, **370**, eaba6118.
42 T. Smolinka, H. Bergmann, J. Garche and M. Kusnezoff, in *Electrochemical Power Sources: Fundamentals, Systems, and Applications*, ed. T. Smolinka and J. Garche, Elsevier, 2022, pp. 83–164.
43 R. Solanki, I. Patra, N. Ahmad, N. B. Kumar, R. M. R. Parra, M. Zaidi, G. Yasin, T. C. Anil Kumar, H. A. Hussein, R. Sivaraman, H. S. Majdi, O. K. A. Alkadir and R. Yaghobi, *J. Environ. Chem. Eng.*, 2022, **10**, 108207.
44 C. Li and J. B. Baek, *ACS Omega*, 2020, **5**, 31–40.
45 T. Naito, T. Shinagawa, T. Nishimoto and K. Takanabe, *Inorg. Chem. Front.*, 2021, **8**, 2900–2917.
46 M. El-Shafie, *Results Eng.*, 2023, **20**, 101426.
47 S. Shiva Kumar and H. Lim, *Energy Rep.*, 2022, **8**, 13793–13813.
48 C. V. Pham, D. Escalera-López, K. Mayrhofer, S. Cherevko and S. Thiele, *Adv. Energy Mater.*, 2021, **11**, 2101998.
49 L. A. King, M. A. Hubert, C. Capuano, J. Manco, N. Danilovic, E. Valle, T. R. Hellstern, K. Ayers and T. F. Jaramillo, *Nat. Nanotechnol.*, 2019, **14**, 1071–1074.
50 M. A. Hubert, L. A. King and T. F. Jaramillo, *ACS Energy Lett.*, 2021, **7**, 17–23.
51 Z. Rui, K. Hua, Z. Dou, A. Tan, C. Zhang, X. Shi, R. Ding, X. Li, X. Duan, Y. Wu, Y. Zhang, X. Wang, J. Li and J. Liu, *J. Mater. Chem. A*, 2024, **12**, 9563–9573.
52 N. Wang, S. Song, W. Wu, Z. Deng and C. Tang, *Adv. Energy Mater.*, 2024, **14**, 2303451.

53 G. F. Swiegers, A. L. Hoang, A. Hodges, G. Tsekouras, C.-Y. Lee, K. Wagner and G. Wallace, *Curr. Opin. Electrochem*, 2022, **32**, 100881.
54 X. Yan, J. Biemolt, K. Zhao, Y. Zhao, X. Cao, Y. Yang, X. Wu, G. Rothenberg and N. Yan, *Nat. Commun.*, 2021, **12**, 4143.
55 G. D. O'Neil, C. D. Christian, D. E. Brown and D. V. Esposito, *J. Electrochem. Soc.*, 2016, **163**, F3012–F3019.
56 P. Hadikhani, S. M. H. Hashemi, S. A. Schenk and D. Psaltis, *Sustainable Energy Fuels*, 2021, **5**, 2419–2432.
57 A. Hodges, A. L. Hoang, G. Tsekouras, K. Wagner, C. Y. Lee, G. F. Swiegers and G. G. Wallace, *Nat. Commun.*, 2022, **13**, 1304.
58 S. M. H. Hashemi, M. A. Modestino and D. Psaltis, *Energy Environ. Sci.*, 2015, **8**, 2003–2009.
59 M. I. Gillespie, F. van der Merwe and R. J. Kriek, *J. Power Sources*, 2015, **293**, 228–235.
60 K. Schoppmann, H. Rox, E. Frense, F. Rüdiger, X. Yang, K. Eckert and J. Fröhlich, *Chem. Eng. J.*, 2025, **507**, 160040.
61 S. Liang, Y. Ma, H. Luo, K. Wu, J. Chen and J. Yang, *Chem. – Eur. J.*, 2023, **29**, e202302160.
62 Capillary-fed electrolysis technology © Hysata, 2024, (**https://hysata.com/our-technology/**).
63 L. Wan, Z. Xu, Q. Xu, M. Pang, D. Lin, J. Liu and B. Wang, *Energy Environ. Sci.*, 2023, **16**, 1384–1430.
64 Q. Xu, L. Zhang, J. Zhang, J. Wang, Y. Hu, H. Jiang and C. Li, *EnergyChem*, 2022, **4**, 100087.
65 Z. W. Seh, J. Kibsgaard, C. F. Dickens, I. Chorkendorff, J. K. Norskov and T. F. Jaramillo, *Science*, 2017, **355**, eaad4998.
66 H. Shi, Y. T. Zhou, R. Q. Yao, W. B. Wan, X. Ge, W. Zhang, Z. Wen, X. Y. Lang, W. T. Zheng and Q. Jiang, *Nat. Commun.*, 2020, **11**, 2940.
67 X. Wang, R. Su, H. Aslan, J. Kibsgaard, S. Wendt, L. Meng, M. Dong, Y. Huang and F. Besenbacher, *Nano Energy*, 2015, **12**, 9–18.
68 S. Saha and A. K. Ganguli, *ChemistrySelect*, 2017, **2**, 1630–1636.
69 K. Qu, Y. Zheng, X. Zhang, K. Davey, S. Dai and S. Z. Qiao, *ACS Nano*, 2017, **11**, 7293–7300.
70 X. Yue, S. Huang, J. Cai, Y. Jin and P. K. Shen, *J. Mater. Chem. A*, 2017, **5**, 7784–7790.
71 A. Sivanantham, P. Ganesan, L. Estevez, B. P. McGrail, R. K. Motkuri and S. Shanmugam, *Adv. Energy Mater.*, 2018, **8**, 1702838.
72 Y. Luo, L. Tang, U. Khan, Q. Yu, H. M. Cheng, X. Zou and B. Liu, *Nat. Commun.*, 2019, **10**, 269.
73 L. Wei, K. Goh, O. Birer, H. E. Karahan, J. Chang, S. Zhai, X. Chen and Y. Chen, *Nanoscale*, 2017, **9**, 4401–4408.
74 T. Ami, K. Oka, H. Kasai and T. Kimura, *Chem. Commun.*, 2025, **61**, 1533–1558.
75 S. Zaman, M. Khalid and S. Shahgaldi, *ACS Energy Lett.*, 2024, **9**, 2922–2935.
76 Y. Yang, H. Yao, Z. Yu, S. M. Islam, H. He, M. Yuan, Y. Yue, K. Xu, W. Hao, G. Sun, H. Li, S. Ma, P. Zapol and M. G. Kanatzidis, *JACS*, 2019, **141**, 10417–10430.
77 Q. Gong, Y. Wang, Q. Hu, J. Zhou, R. Feng, P. N. Duchesne, P. Zhang, F. Chen, N. Han, Y. Li, C. Jin, Y. Li and S. T. Lee, *Nat. Commun.*, 2016, **7**, 13216.
78 S. Pattaweepaiboon, P. Samarungkasut, P. Iamprasertkun, P. Arkasalerks, K. Nueangnoraj, A. Boonchun, A. Pumsantier, W. Hirunpinyopas and W. Sirisaksoontorn, *ACS Appl. Nano Mater.*, 2024, **8**, 438–448.
79 C. Tsounis, B. Subhash, P. V. Kumar, N. M. Bedford, Y. Zhao, J. Shenoy, Z. Ma, D. Zhang, C. Y. Toe, S. Cheong, R. D. Tilley, X. Lu, L. Dai, Z. Han and R. Amal, *Adv. Funct. Mater.*, 2022, **32**, 2203067.
80 L. Quan, H. Jiang, G. Mei, Y. Sun and B. You, *Chem. Rev.*, 2024, **124**, 3694–3812.
81 Y. Luo, Z. Zhang, M. Chhowalla and B. Liu, *Adv. Mater.*, 2022, **34**, e2108133.
82 H. Wu, Q. Huang, Y. Shi, J. Chang and S. Lu, *Nano Res.*, 2023, **16**, 9142–9157.
83 R. Wan, T. Yuan, L. Wang, B. Li, M. Liu and B. Zhao, *Nat. Catal*, 2024, **7**, 1288–1304.
84 F. Liu, C. Shi, X. Guo, Z. He, L. Pan, Z. F. Huang, X. Zhang and J. J. Zou, *Adv. Sci.*, 2022, **9**, e2200307.
85 J. Shi, Y. Bao, R. Ye, J. Zhong, L. Zhou, Z. Zhao, W. Kang and S. B. Aidarova, *Catal. Sci. Technol.*, 2025, 2104–2131.
86 W. Zheng, L. Y. S. Lee and K. Y. Wong, *Nanoscale*, 2021, **13**, 15177–15187.
87 J. Tang, C. Su and Z. Shao, *Exploration*, 2024, **4**, 20220112.
88 X. Zhao, H. Ren and L. Luo, *Langmuir*, 2019, **35**, 5392–5408.
89 A. Angulo, P. van der Linde, H. Gardeniers, M. Modestino and D. Fernández Rivas, *Joule*, 2020, **4**, 555–579.
90 L. Yu, Y. Yang, P. Xie, Q. Xu, A. Kumar, L. Luo, H. Li, H. Xu, H. Duan and X. Sun, *EES Catal.*, 2025, **3**, 152–160.
91 P. Tiwari, G. Tsekouras, K. Wagner, G. F. Swiegers and G. G. Wallace, *Int. J. Hydrogen Energy*, 2019, **44**, 23568–23579.
92 K. Deng, H. Feng, Y. Zhang, D. Liu and Q. Li, *Joule*, 2023, **7**, 1852–1866.
93 H. Vogt, *Electrochim. Acta*, 2017, **235**, 495–499.
94 Y. Li, G. Yang, S. Yu, Z. Kang, J. Mo, B. Han, D. A. Talley and F.-Y. Zhang, *Int. J. Hydrogen Energy*, 2019, **44**, 28283–28293.
95 A. M. Meulenbroek, A. W. Vreman and N. G. Deen, *Electrochim. Acta*, 2021, **385**, 138298.
96 H. Zhang, Y. Ma, M. Huang, G. Mutschke and X. Zhang, *Soft Matter*, 2024, **20**, 3097–3106.
97 X. Yang, D. Baczyzmalski, C. Cierpka, G. Mutschke and K. Eckert, *Phys. Chem. Chem. Phys.*, 2018, **20**, 11542–11548.
98 S. Park, L. Liu, C. Demirkir, O. van der Heijden, D. Lohse, D. Krug and M. T. M. Koper, *Nat. Chem.*, 2023, **15**, 1532–1540.
99 Q. Chen, J. Zhao, X. Deng, Y. Shan and Y. Peng, *J. Phys. Chem. Lett.*, 2022, **13**, 6153–6163.
100 M. Suvira, A. Ahuja, P. Lovre, M. Singh, G. W. Draher and B. Zhang, *Anal. Chem.*, 2023, **95**, 15893–15899.
101 L. Ding, W. Wang, Z. Xie, K. Li, S. Yu, C. B. Capuano, A. Keane, K. Ayers and F. Y. Zhang, *ACS Appl. Mater. Interfaces*, 2023, **15**, 24284–24295.
102 Y. Kang, S. Lee, S. Han, D. Jeon, M. Bae, Y. Choi, D. W. Lee and J. Ryu, *Adv. Funct. Mater.*, 2024, **34**, 2308827.
103 V. B. Svetovoy, R. G. Sanders and M. C. Elwenspoek, *J. Phys.: Condens. Matter*, 2013, **25**, 184002.
104 M. Mita, H. Matsushima, M. Ueda and H. Ito, *J. Colloid Interface Sci.*, 2022, **614**, 389–395.

105 D. Lohse and X. Zhang, *Phys. Rev. E: Stat., Nonlinear, Soft Matter Phys.*, 2015, **91**, 031003.
106 Y. Zhang, X. Zhu, J. A. Wood and D. Lohse, *Proc. Natl. Acad. Sci. U. S. A.*, 2024, **121**, e2321958121.
107 H. Wang, Z. Xu, W. Lin, X. Yang, X. Gu, W. Zhu and Z. Zhuang, *Nano Res.*, 2022, **16**, 420–426.
108 W. Xu, Z. Lu, X. Sun, L. Jiang and X. Duan, *Acc. Chem. Res.*, 2018, **51**, 1590–1598.
109 L. Wan, Z. Xu, Q. Xu, P. Wang and B. Wang, *Energy Environ. Sci.*, 2022, **15**, 1882–1892.
110 T. Kou, S. Wang, R. Shi, T. Zhang, S. Chiovoloni, J. Q. Lu, W. Chen, M. A. Worsley, B. C. Wood, S. E. Baker, E. B. Duoss, R. Wu, C. Zhu and Y. Li, *Adv. Energy Mater.*, 2020, **10**, 2002955.
111 J. Das, S. Mandal, A. Borbora, S. Rani, M. Tenjimbayashi and U. Manna, *Adv. Funct. Mater.*, 2023, 2311648.
112 R. Xu, L. Du, D. Adekoya, G. Zhang, S. Zhang, S. Sun and Y. Lei, *Adv. Energy Mater.*, 2020, **11**, 2001537.
113 H. Fan, S. Zhou, Q. Wei and X. Hu, *Renewable Sustainable Energy Rev.*, 2022, **165**, 112585.
114 H. H. Lin, C. H. Lin and S. C. Luo, *ACS Appl. Mater. Interfaces*, 2023, **15**, 29214–29223.
115 J. Kim, S. M. Jung, N. Lee, K. S. Kim, Y. T. Kim and J. K. Kim, *Adv. Mater.*, 2023, **35**, 2305844.
116 Q. Ren, L. Feng, C. Ye, X. Xue, D. Lin, S. Eisenberg, T. Kou, E. B. Duoss, C. Zhu and Y. Li, *Adv. Energy Mater.*, 2023, **13**, 2302073.
117 D. Wang, L. Liu, Y. Liu, W. Luo, Y. Xie, T. Xiao, Y. Wang, Z. Song, H. Zhang and X. Wang, *ACS Sustainable Chem. Eng.*, 2023, **11**, 16479–16490.
118 M. Bae, Y. Kang, D. W. Lee, D. Jeon and J. Ryu, *Adv. Energy Mater.*, 2022, **12**, 2201452.
119 O. Winther-Jensen, K. Chatjaroenporn, B. Winther-Jensen and D. R. MacFarlane, *Int. J. Hydrogen Energy*, 2012, **37**, 8185–8189.
120 X. Dai, W. Si, Y. Liu, W. Zhang and Z. Guo, *ACS Appl. Mater. Interfaces*, 2024, **16**, 11984–11996.
121 J. Li, Y. Zhu, W. Chen, Z. Lu, J. Xu, A. Pei, Y. Peng, X. Zheng, Z. Zhang, S. Chu and Y. Cui, *Joule*, 2019, **3**, 557–569.
122 C. Yu, M. Cao, Z. Dong, K. Li, C. Yu, J. Wang and L. Jiang, *Adv. Funct. Mater.*, 2016, **26**, 6830–6835.
123 J. Zhang, F. Dong, C. Wang, J. Wang, L. Jiang and C. Yu, *ACS Appl. Mater. Interfaces*, 2021, **13**, 32435–32441.
124 Z. Long, Y. Zhao, C. Zhang, Y. Zhang, C. Yu, Y. Wu, J. Ma, M. Cao and L. Jiang, *Adv. Mater.*, 2020, **32**, 1908099.
125 S. Roy, U. Qamar, A. A. Sasikala Devi and S. Das, *APL Energy*, 2024, **2**, 011504.
126 Y. Li, H. Zhang, N. Han, Y. Kuang, J. Liu, W. Liu, H. Duan and X. Sun, *Nano Res.*, 2018, **12**, 177–182.
127 Z. Long, C. Yu, M. Cao, J. Ma and L. Jiang, *Adv. Mater.*, 2024, **36**, e2312179.
128 P. Trogadas and M. O. Coppens, *Chem. Soc. Rev.*, 2020, **49**, 3107–3141.
129 M. N. MacGregor-Ramiasa and K. Vasilev, *Adv. Mater. Interfaces*, 2017, **4**, 1700381.
130 C. Zhang, C. Teng, S. Guo, Y. Sun, C. Yu, X. Jin, K. Liu and L. Jiang, *Nano Lett.*, 2024, **24**, 1959–1966.
131 Y. Dong, H. Wang, X. Wang, H. Wang, Q. Dong, W. Wang, X. Wei, J. Ren, J. Liu and R. Wang, *Chem. Eng. J.*, 2024, **488**, 150953.
132 C. Zhang, Z. Xu, N. Han, Y. Tian, T. Kallio, C. Yu and L. Jiang, *Sci. Adv.*, 2023, **9**, eadd6978.
133 S. Sheng, B. Shi, C. Wang, L. Luo, X. Lin, P. Li, F. Chen, Z. Shang, H. Meng, Y. Kuang, W. F. Lin and X. Sun, *ACS Appl. Mater. Interfaces*, 2020, **12**, 23627–23634.
134 I. Morcos, *J. Electroanal. Chem. Interfacial Electrochem.*, 1975, **62**, 313–340.
135 H. Qiu, K. Obata, Z. Yuan, T. Nishimoto, Y. Lee, K. Nagato, I. Kinefuchi, J. Shiomi and K. Takanabe, *Langmuir*, 2023, **39**, 4993–5001.
136 J. da Silva, E. Nobrega, F. Staciaki, F. R. Almeida, G. Wosiak, A. Gutierrez, O. Bruno, M. C. Lopes and E. Pereira, *Chem. Eng. J.*, 2024, **494**, 152943.
137 X. Lu, D. Yadav, B. Ma, L. Ma and D. Jing, *J. Power Sources*, 2024, **599**, 234217.
138 A. F. M. Mahrous, I. M. Sakr, A. Balabel and K. Ibrahim, *Int. J. Ther. Environ. Eng.*, 2010, **2**, 113–116.
139 S. J. Hendel and E. R. Young, *J. Chem. Educ.*, 2016, **93**, 1951–1956.
140 B. Bensmann and R. Hanke-Rauschenbach, *ECS Trans.*, 2016, **75**, 1065.
141 G. Schmidt, M. Suermann, B. Bensmann, R. Hanke-Rauschenbach and I. Neuweiler, *J. Electrochem. Soc.*, 2020, **167**, 114511.
142 D. Grondin, J. Deseure, P. Ozil, J. P. Chabriat, B. Grondin-Perez and A. Brisse, *J. Power Sources*, 2011, **196**, 9561–9567.
143 J. K. Lee, C. H. Lee and A. Bazylak, *J. Power Sources*, 2019, **437**, 226910.
144 J. K. Lee and A. Bazylak, *J. Electrochem. Soc.*, 2020, **167**, 013541.
145 R. Ding, Y. Chen, Z. Rui, K. Hua, Y. Wu, X. Li, X. Duan, J. Li, X. Wang and J. Liu, *J. Power Sources*, 2023, **556**, 232389.
146 X. Chen, A. Rex, J. Woelke, C. Eckert, B. Bensmann, R. Hanke-Rauschenbach and P. Geyer, *Appl. Energy*, 2024, **371**, 123550.
147 S. Hu, B. Guo, S. Ding, F. Yang, J. Dang, B. Liu, J. Gu, J. Ma and M. Ouyang, *Appl. Energy*, 2022, **327**, 120099.
148 D. S. Falcão and A. M. F. R. Pinto, *J. Cleaner Prod.*, 2020, **261**, 121184.
149 C. Daoudi and T. Bounahmidi, *Int. J. Hydrogen Energy*, 2024, **49**, 646–667.
150 S. K. Sarma, A. Singh, R. Mohan and A. Shukla, *Int. J. Hydrogen Energy*, 2023, **48**, 17769–17782.
151 H. H. Girault, *Analytical and physical electrochemistry*, EPFL Press, 2004.
152 C. G. Zoski, *Handbook of electrochemistry*, Elsevier, 2006.
153 O. van der Heijden, S. Park, R. E. Vos, J. J. J. Eggebeen and M. T. M. Koper, *ACS Energy Lett.*, 2024, **9**, 1871–1879.
154 A. Taqieddin, R. Nazari, L. Rajic and A. Alshawabkeh, *J. Electrochem. Soc.*, 2017, **164**, E448–E459.

155 A. Taqieddin, M. R. Allshouse and A. N. Alshawabkeh, *J. Electrochem. Soc.*, 2018, **165**, E694–E711.
156 Z. Zhang, W. Liu and M. L. Free, *J. Electrochem. Soc.*, 2019, **167**, 013532.
157 F. F. Rivera, T. Pérez, L. F. Castañeda and J. L. Nava, *Chem. Eng. Sci.*, 2021, **239**, 116622.
158 F. Khalighi, N. G. Deen, Y. Tang and A. W. Vreman, *Chem. Eng. Sci.*, 2023, **267**, 118280.
159 Z. Lu, L. Zhang, R. Iwata, E. N. Wang and J. C. Grossman, *Langmuir*, 2020, **36**, 15112–15118.
160 N. Varallo, G. Besagni and R. Mereu, *Chem. Eng. Sci.*, 2023, **280**, 119090.
161 S. Subramaniam, *Prog. Energy Combust. Sci.*, 2013, **39**, 215–245.
162 J. Schillings, O. Doche and J. Deseure, *Int. J. Heat Mass Transfer*, 2015, **85**, 292–299.
163 D. Le Bideau, P. Mandin, M. Benbouzid, M. Kim, M. Sellier, F. Ganci and R. Inguanta, *Energies*, 2020, **13**, 3394.
164 W. Yang, L. Sun, J. Tang, Z. Mo, H. Liu, M. Du and J. Bao, *Ind. Eng. Chem. Res.*, 2022, **61**, 8323–8332.
165 X. Pang, J. T. Davis, A. D. Harvey and D. V. Esposito, *Energy Environ. Sci.*, 2020, **13**, 3663–3678.
166 T. L. Doan, H. E. Lee, S. S. H. Shah, M. Kim, C. H. Kim, H. S. Cho and T. Kim, *Int. J. Energy Res.*, 2021, **45**, 14207–14220.
167 Q. Chen, Y. Wang, F. Yang and H. Xu, *Int. J. Hydrogen Energy*, 2020, **45**, 32984–32994.
168 J. A. Wrubel, Z. Kang, L. Witteman, F.-Y. Zhang, Z. Ma and G. Bender, *Int. J. Hydrogen Energy*, 2021, **46**, 25341–25354.
169 C. C. Weber, T. Schuler, R. De Bruycker, L. Gubler, F. N. Büchi and S. De Angelis, *J. Power Sources Adv.*, 2022, **15**, 100095.
170 A. Nouri-Khorasani, E. Tabu Ojong, T. Smolinka and D. P. Wilkinson, *Int. J. Hydrogen Energy*, 2017, **42**, 28665–28680.
171 Y. Li, Z. Kang, J. Mo, G. Yang, S. Yu, D. A. Talley, B. Han and F.-Y. Zhang, *Int. J. Hydrogen Energy*, 2018, **43**, 11223–11233.
172 M. Maier, K. Smith, J. Dodwell, G. Hinds, P. R. Shearing and D. J. L. Brett, *Int. J. Hydrogen Energy*, 2022, **47**, 30–56.
173 J. Nie and Y. Chen, *Int. J. Hydrogen Energy*, 2010, **35**, 3183–3197.
174 J. Zheng, Z. Kang, B. Han and J. Mo, *Materials*, 2023, **16**, 1310.
175 A. Ni, M. Upadhyay, S. S. Kumar, H. Uwitonze and H. Lim, *Int. J. Hydrogen Energy*, 2023, **48**, 16176–16183.
176 W. Wang, B. Han, B. Cao and J. Mo, *Int. J. Hydrogen Energy*, 2023, **48**, 36240–36253.
177 M. Zhang, L. Gao, L. Yang, G. Shan, Y. Wang, X. Huo, W. Li and J. Zhang, *Fuel*, 2024, **367**, 131418.
178 P. Dyson, R. Ransing, P. H. Williams and R. Williams, *Fluid properties at nano/meso scale: a numerical treatment*, John Wiley & Sons, 2008.
179 L. Chen, A. He, J. Zhao, Q. Kang, Z.-Y. Li, J. Carmeliet, N. Shikazono and W.-Q. Tao, *Prog. Energy Combust. Sci.*, 2022, **88**, 100968.
180 L. Chen, R. Zhang, Q. Kang and W.-Q. Tao, *Chem. Eng. J.*, 2020, **391**, 123590.
181 M. El Hannach, M. Prat and J. Pauchet, *Int. J. Hydrogen Energy*, 2012, **37**, 18996–19006.
182 L. Chen, Q. Kang and W. Tao, *Int. J. Hydrogen Energy*, 2021, **46**, 13283–13297.
183 M. Shahraeeni and M. Hoorfar, *Int. J. Hydrogen Energy*, 2014, **39**, 10697–10709.
184 H. Nakajima, S. Iwasaki and T. Kitahara, *J. Power Sources*, 2023, **560**, 232677.
185 T. Seip, N. Shaigan, M. Dinu, K. Fatih and A. Bazylak, *J. Power Sources*, 2023, **559**, 232654.
186 B. Tjaden, S. J. Cooper, D. J. L. Brett, D. Kramer and P. R. Shearing, *Curr. Opin. Chem. Eng.*, 2016, **12**, 44–51.
187 M. Ebner and V. Wood, *J. Electrochem. Soc.*, 2015, **162**, A3064–A3070.
188 B. Tjaden, D. J. L. Brett and P. R. Shearing, *Int. Mater. Rev.*, 2016, **63**, 47–67.
189 G. Li, M. Xu, Y. Qin, Y. Zhang, Y. Wang, X. Yu and J. Li, *Fuel*, 2024, **368**, 131444.
190 M. F. Kaya and N. Demir, *Fuel Cells*, 2017, **17**, 37–47.
191 M. T. de Groot, J. Kraakman and R. L. Garcia Barros, *Int. J. Hydrogen Energy*, 2022, **47**, 34773–34783.
192 M. Chandesris, V. Médeau, N. Guillet, S. Chelghoum, D. Thoby and F. Fouda-Onana, *Int. J. Hydrogen Energy*, 2015, **40**, 1353–1366.
193 B. Han, S. M. Steen, J. Mo and F.-Y. Zhang, *Int. J. Hydrogen Energy*, 2015, **40**, 7006–7016.
194 V. Liso, G. Savoia, S. S. Araya, G. Cinti and S. K. Kær, *Energies*, 2018, **11**, 3273.
195 X. Qian, K. Kim and S. Jung, *Energy Convers. Manage.*, 2022, **268**, 116070.
196 Y. Jiang, Y. Li, Y. Ding, S. Hu, J. Dang, F. Yang and M. Ouyang, *J. Power Sources*, 2023, **553**, 232303.
197 D. Huang, Z. Zhong, X. Ai, K. Hu, B. Xiong, Q. Wen, J. Fang and S. Cheng, *Energy Convers. Manage.*, 2024, **300**, 117955.
198 M. Espinosa-López, C. Darras, P. Poggi, R. Glises, P. Baucour, A. Rakotondrainibe, S. Besse and P. Serre-Combe, *Renewable Energy*, 2018, **119**, 160–173.
199 Z. Ren, J. Wang, Z. Yu, C. Zhang, S. Gao and P. Wang, *J. Power Sources*, 2022, **544**, 231886.
200 A. Rajora and J. W. Haverkort, *J. Power Sources*, 2022, **260**, 117823.
201 X. Guo, H. Zhu and S. Zhang, *Int. J. Hydrogen Energy*, 2024, **49**, 1048–1059.
202 M. G. Rasul, M. A. Hazrat, M. A. Sattar, M. I. Jahirul and M. J. Shearer, *Energy Convers. Manage.*, 2022, **272**, 116326.
203 D. Tonelli, L. Rosa, P. Gabrielli, K. Caldeira, A. Parente and F. Contino, *Nat. Commun.*, 2023, **14**, 5532.
204 S. Krishnan, V. Koning, M. Theodorus de Groot, A. de Groot, P. G. Mendoza, M. Junginger and G. J. Kramer, *Int. J. Hydrogen Energy*, 2023, **48**, 32313–32330.
205 R. J. Ouimet, J. R. Glenn, D. De Porcellinis, A. R. Motz, M. Carmo and K. E. Ayers, *ACS Catal.*, 2022, **12**, 6159–6171.
206 M. Clapp, C. M. Zalitis and M. Ryan, *Catal. Today*, 2023, **420**, 114140.

207 IRENA, *World Energy Transitions Outlook 2022: 1.5 °C Pathway*, International Renewable Energy Agency, Abu Dhabi, 2022.
208 X. Fu, R. Shi, S. Jiao, M. Li and Q. Li, *J. Energy Chem.*, 2022, **70**, 129–153.
209 E. Urbano, E. Pahon, N. Yousfi-Steiner and M. Guillou, *J. Power Sources*, 2024, **623**, 235451.
210 E. Kuhnert, V. Hacker, M. Bodner and P. Subramanian, *Int. J. Energy Res.*, 2023, **2023**, 1–23.
211 F. N. Khatib, T. Wilberforce, O. Ijaodola, E. Ogungbemi, Z. El-Hassan, A. Durrant, J. Thompson and A. G. Olabi, *Renewable Sustainable Energy Rev.*, 2019, **111**, 1–14.
212 F. Meharban, C. Lin, X. Wu, L. Tan, H. Wang, W. Hu, D. Zhou, X. Li and W. Luo, *Adv. Energy Mater.*, 2024, 2402886.
213 M. Möckl, M. F. Ernst, M. Kornherr, F. Allebrod, M. Bernt, J. Byrknes, C. Eickes, C. Gebauer, A. Moskovtseva and H. A. Gasteiger, *J. Electrochem. Soc.*, 2022, **169**, 064505.
214 L. Messing, K. Pellumbi, L. Hoof, N. Imming, S. Wilbers, L. Kopietz, M. Joemann, A. Grevé, K. Junge Puring and U. P. Apfel, *Adv. Energy Mater.*, 2024, 2402308.
215 R. A. Marquez, M. Espinosa, E. Kalokowski, Y. J. Son, K. Kawashima, T. V. Le, C. E. Chukwuneke and C. B. Mullins, *ACS Energy Lett.*, 2024, **9**, 547–555.
216 J. C. Ehlers, A. A. Feidenhans'l, K. T. Therkildsen and G. O. Larrazábal, *ACS Energy Lett.*, 2023, **8**, 1502–1509.
217 Y. Devi, P. J. Huang, W. T. Chen, R. H. Jhang and C. H. Chen, *ACS Appl. Energy Mater.*, 2023, **15**, 9231–9239.
218 H. Becker, J. Murawski, D. V. Shinde, I. E. L. Stephens, G. Hinds and G. Smith, *Sustainable Energy Fuels*, 2023, **7**, 1565–1603.
219 M. Demnitz, Y. M. Lamas, R. L. Garcia Barros, A. de Leeuw den Bouter, J. van der Schaaf and M. Theodorus de Groot, *iScience*, 2024, **27**, 108695.
220 L. Liu, H. Ma, M. Khan and B. S. Hsiao, *Membranes*, 2024, **14**, 85.
221 Z. Tang, B. Wu, K. Yan, J. Luo, M. U. Haq and L. Zeng, *Future Batteries*, 2025, **5**, 100024.
222 U. K. Ghorui, G. Sivaguru, U. B. Teja, A. M, S. Ramakrishna, S. Ghosh, G. K. Dalapati and S. Chakrabortty, *ACS Appl. Energy Mater.*, 2024, **7**, 7649–7676.
223 G. A. Jones and K. J. Warner, *Energy Policy*, 2016, **93**, 206–212.

